

This work is on a Creative Commons Attribution-NonCommercial-NoDerivatives 4.0 International (CC BY-NC-ND 4.0) license, <https://creativecommons.org/licenses/by-nc-nd/4.0/>. Access to this work was provided by the University of Maryland, Baltimore County (UMBC) ScholarWorks@UMBC digital repository on the Maryland Shared Open Access (MD-SOAR) platform.

Please provide feedback Please support the ScholarWorks@UMBC repository by emailing scholarworks-group@umbc.edu and telling us what having access to this work means to you and why it's important to you. Thank you.

**Pre-operative Assessment of Ablation Margins for Variable Blood Perfusion
Metrics in a Magnetic Resonance Imaging Based Complex Breast Tumour
Anatomy: Simulation Paradigms in Thermal Therapies**

Manpreet Singh^{a,c,d,*}, Tulika Singh^b, Sanjeev Soni^c

^aDepartment of Mechanical Engineering, University of Maryland Baltimore County, Baltimore, Maryland, USA; ^bDepartment of Radio-diagnosis and Imaging, Post Graduate Institute of Medical Education and Research, Chandigarh, India; ^cBiomedical Instrumentation Division, CSIR-Central Scientific Instruments Organisation, Chandigarh, India; ^dDepartment of Mechanical Engineering, Thapar Institute of Engineering and Technology University, Patiala, Punjab, India.

***Correspondence to:**

Manpreet Singh, Ph.D (P), M.E.

Department of Mechanical Engineering,

College of Engineering and Information Technology,

University of Maryland Baltimore County,

1000 Hilltop Circle, Baltimore, MD 21250, United States.

Phone: +1-(908) 405-7554; E-mail: snamra.manpreet@gmail.com

Journal: Computer Methods and Programs in Biomedicine

Cover Title: Perfusion Mediated Assessment of Ablation Margins

ABSTRACT

Background and Objectives: Image-guided medical interventions facilitates precise visualization at treatment site. The conformal prediction for sparing healthy tissue fringes precisely in the vicinity of irregular tumour anatomy remains clinically challenging. Pre-clinical image-based computational modelling is imperative as it helps in enhancement of treatment quality, augmenting clinical-decision making, while planning, targeting, controlling, monitoring and assessing treatment response with an effective risk assessment before the onset of treatment in clinical settings. In this study, the influence of heat deposition rate (SAR), exposure duration, and variable blood perfusion metrics for a patient-specific breast tumour is quantified considering the tumour margins thereby suggesting need of geometrically accurate models.

Methods: A three-dimensional realistic model mimicking dimensions of a female breast, comprising ~1.7 cm irregular tumour, was generated from patient specific two-dimensional DICOM format MRI images through image segmentation tools MIMICS 19.0® and 3-Matic 11.0® which is finally exported to COMSOL Multiphysics 5.2® as a volumetric mesh for finite element analysis. The Pennes bioheat transfer model and Arrhenius thermal damage model of cell-death are integrated to simulate a coupled biophysics problem. A comparative blood perfusion analysis is done to evaluate the response of tumour during heating considering thermal damage extent, including the tumour margins while sparing critical adjoining healthy tissues.

Results: The evaluated thermal damage zones for 1 mm, 2 mm and 3 mm fringe heating region (beyond tumour boundary) reveals 0.09%, 0.21% and 0.34% thermal damage to the healthy tissue (which is <1%) and thus successful necrosis of the tumour. The iterative computational experiments suggests treatment margins < 5 mm are sufficient enough as heating beyond 3 mm fringe layer leads to higher damage surrounding the tumour approximately 1.5 times the tumour volume. Further, the heat-dosage requirements are 22% more for highly perfused tumour as compared to moderately perfused tumour with an approximate double time to ablate the whole tumour volume.

Conclusions: Depending on the blood perfusion characteristics of a tumour, it is a trade-off between heat-dosage (SAR) and exposure/treatment duration to get desired thermal damage including the irregular tumour boundaries while taking into account, the margin of healthy tissue. The suggested patient-specific integrated multiphysics-model based on MRI-Images may be implemented for pre-treatment planning based on the tumour blood perfusion to evaluate the thermal ablation zone dimensions clinically and thereby avoiding the damage of off-target tissues. Thus, risks involving underestimation or overestimation of thermal coagulation zones may be minimised while preserving the surrounding normal breast parenchyma.

Keywords: Thermal therapy; Bioheat transfer; Patient-specific reconstruction; Breast tumour perfusion; Treatment margins; Thermal damage.

1. Introduction

In medical oncology, quantification of tumour safety margins always remains erratic and arbitrary, as it may not reflect true or actual distance for tissue fringes beyond the boundary of tumour that needs to be sacrificed. Furthermore, there is an inextricable connectivity between the tumour and surrounding healthy tissue that makes this quantitative assessment even more arduous and challenging for the cases where no safety margins can be found. Thus, the prediction for sparing healthy tissue margins/extents, around a tumour, remains a challenge for available cancer treatment modalities including the thermal ablation methods [1]. Generally, wider margins beyond tumour boundary are sacrificed to avoid recurrence of cancer. These tumour margins are generally referred to as “security rim” and approximate value of 0.5-1 cm is reported in literature [2-5].

Magnetic nanoparticle-assisted thermal therapy (MNATT) is a minimally invasive non-surgical cancer treatment that uses heat, induced by nanoparticles to kill tumour cells and desired tumour margins. In MNATT, a tumour embedded with magnetic nanoparticles, is subjected to an alternating magnetic field of certain frequency to induce irreversible thermal damage to diseased tissue. For such a therapy it is necessary to understand the heat-induced cell-death for a tumour and the healthy tissue fringes that needs to be sacrificed with heat conduction. This help in identifying under-heating within tumour periphery and overheating/hot-spots in surrounding healthy tissue especially for irregular tumour shape. As of now, there lacks studies that can establish a link between three-dimensional pre-operative planning and post-operative assessment to quantify accurate tumour margins and thermally ablative fringes [6]. Accurate determination of tumour margins enables a physician to deliver controlled heat and exposure to maintain the desired tumour margins in close proximity to tumours.

Furthermore, the decisions about tumour margins are widely impacted by the clinical imaging information. This patient-specific tumour information obtained through magnetic resonance imaging (MRI), computed tomography (CT) etc. thus can be used to generate a three-dimensional model [7-9]. Image-based tumour computations improve the treatment efficacy opting for suitable clinical treatment parameters like SAR for magnetic nanoparticle thermal therapy.

The scope of this manuscript spans towards patient-specific tumour anatomy and implications of variable blood perfusion for evaluating the temperature distribution and thermal damage considering the tumour margins to specify blood perfusion based SAR and exposure durations for an irregular (real) tumour geometry. By incorporating various blood perfusion conditions, for moderately and highly perfused tumour, the thermal damage zones especially at irregular region of tumour are estimated while ensuring minimal damage to surrounding healthy tissue. Accordingly, thermal energy deposition i.e. SAR value and exposure duration are specified for the considered size of breast tumour to attain desired necrosis volume for two blood

perfusion cases. The ultimate goal is to improve precision while accurately determining the tumour margins with the aid of medical-imaging assisted computational analysis.

2. Materials and Methods

Simulations performed for hyperthermia sessions can be grouped into three distinct important tasks [10-15]

1. Generation of patient model based upon the accuracy of obtained MRI/CT/MRA/Micro-CT scan to generate more uniform computational domain (Geometry);
2. Pre-calculations for the distribution of power deposition in the tissue under analysis Specific Absorption Rate (SAR) in tumour, Metabolic heat generation (Q_m) [16-17];
3. Spatiotemporal thermal distribution and thermal damage patterns within (ROI) region of interest: tumour core, interface (fringe heating zone~0-10 mm security rim) [2-3, 9, 18-20, 63-64];
 - a. Identification of hot-spots to minimize collateral thermal damage [21]; temporal variation of blood perfusion as a function of thermal damage [22-23].
 - b. Perfusion dynamics consideration (constant, variable (zero, low, moderate, high)) and mapping of thermo-physiological properties onto spatial coordinates [24].

2.1 Patient specific 3D anatomical model generation

Clinical breast MRI examination was performed at Post Graduate Institute of Medical Education and Research, Chandigarh, India with 1.5 Tesla (Siemens MAGNETOM Aera) using a standard and consistent clinical breast MRI protocol. One woman was imaged in the prone position using a dedicated multichannel surface array breast coil. After the native scan was obtained, Dynamic contrast-enhanced sequences (DCE) were acquired in axial plane employing 3D T1- weighed fast gradient echo-based DCE series with one pre and three post-gadolinium (dose of 0.01 m-mol kg⁻¹) contrast-enhanced sequences. The technical parameters employed were, Plane: axial, 8 channel breast coil, 3D mode, SPIR fat suppression, Parallel imaging Factor 1.5 R/L, TR- 5.6 ms, TE-3 ms, Slice thickness of 1 mm and a flip angle of 10 degrees. The obtained set of DICOM images were used to locate the position and shape of the breast tumour. The reconstruction of complex multi-part geometries from the DICOM-compatible cross-sectional slices is difficult to incorporate due to inconsistencies caused due to face parameterization, and geometry decomposition errors. Till date, most of the previous reported studies had compromised the accuracy of the models by approximating the true shape of irregular biological tissues [23, 25-28]. Probably, our is the first reported work in context of breast cancer to address realistic three-dimensional irregular tumour geometry extracted from MRI scan.

The process of creating the multipart complex geometry from two-dimensional DICOM (Digital Imaging and Communications in Medicine) images sets is illustrated in Supplement file (section-1 Figs. S1 and S2). Two compartment model consisting of tumour and healthy breast was thus constructed from 108 images of MRI scan.

The DICOM format data of MRI images was first imported into MIMICS 19.0® (Materialise's Interactive Medical Image Control System), (Materialise, Leuven, Belgium) for pre-processing prior to implementing simulation in COMSOL-Multiphysics 5.2® (Comsol AB, Stockholm, Sweden). Regions of interest were identified by different gray scale values (pixel values) for each identified tissue. Imported image slices were first cleaned with Gaussian filters to remove background noise and then segmented to identify the breast tumour and healthy fat tissue by selecting image contrast boundaries through thresholding operation for pixel values. Then the region growing (slice by slice) or dynamic region growing (extends the segmentation mask to other slices) operation was performed to eliminate noise and parts that were not connected. This operation enabled differentiation of tumour from the tissue by categorizing them with different masks. After threshold selection, the masks were subsequently used in a flood-fill operation during the reconstruction of the model. Thereafter, the model was meshed in 3-Matic 11.0® to get surface layers for defining the boundary for use by COMSOL (Finite Element Method) packages. Quality of surface layers was further improved by applying morphology operations (Erode, Dilate) and techniques such as smoothing, stitching, wrapping, filling holes and triangle reduction to eliminate bad contours, intersecting and overlapping triangles, noise shells, planar holes and the inverted normal to facilitate error free computing. In this study, we have performed surface-volumetric meshing and exported the mesh geometry as .mphtxt file to COMSOL-Multiphysics 5.2® and subsequently defined the material properties to the model domains. Linear interpolation and constant extrapolation were used to achieve smooth volumetric heat generation and to remove any incurring singularities. The constructed patient-specific two compartment breast model, including the tumour is shown in figs. 1 and 2. The white cloud appearance of tumour, in fig. 1, represents the pixel locations where the density was significantly higher than the healthy fat tissue as appeared during MRI scan [29].

2.2. Computation of spatiotemporal temperatures

Pennes bio-heat equation [30] was used to model the heat transfer to compute spatio-temporal distribution of temperature within the domains i.e. breast tumour and healthy breast tissue, as per Eqs. (1) and (2).

$$\rho_t c_t \frac{\partial T_t}{\partial t} = k_t \nabla^2 T_t + \rho_b c_b \omega_t (T_b - T_t) + Q_{met}^t \quad (1)$$

$$\rho_c c_c \frac{\partial T_c}{\partial t} = k_c \nabla^2 T_c + \rho_b c_b \omega_c (T_b - T_c) + Q_{met}^c + Q_{source}^c \quad (2)$$

Here, T is temperature of tissue, k is thermal conductivity of tissue, ρ_b is density of blood, ω is blood perfusion rate, t is exposure duration, c_b is specific heat capacity of blood, T_b is arterial blood temperature (37°C), Q_{met}^t and Q_{met}^c are amount of energy generated by metabolic processes within tissue and tumour (where superscript t denotes healthy tissue and c denotes cancerous tumour) respectively. Q_{source}^c is the heat generation due to magnetic field and nanoparticle interaction. Thermal and physiological properties of different materials considered in the present study are shown in **Table I**.

Table I: Material, thermal and physiological properties of breast tissue

Parameter	Symbol	Type of Tissue		
		Breast Fat	Breast tumour	Blood
Thermal conductivity, [Wm ⁻¹ K ⁻¹]	k	0.21 ^[16]	0.48 ^[16]	0.52 ^[8]
Density, [kgm ⁻³]	ρ	920 ^[32]	1080 ^[34]	1060 ^[16]
Specific heat, [Jkg ⁻¹ K ⁻¹]	c	3000 ^[32]	3500 ^[32]	4200 ^[16]
Blood perfusion, [s ⁻¹]	ω_b	* 4 × 10 ⁻³ ^[35] ** 8.3 × 10 ⁻³ ^[33]	* 2.1 × 10 ⁻² ^[35] ** 5 × 10 ⁻⁴ ^[33]	----
Metabolic heat, [Wm ⁻³]	Q_{met}	400 ^[16]	10936.45 [#]	----

Source: * highly perfused tissue
 ** moderately perfused tissue
 # calculated values from relation defined by [16-17].

As the tumour shape is irregular, the tumour diameter was calculated by averaging the information obtained from three principle planes X-Y (Axial), Y-Z (Sagittal), X-Z (Coronal) as shown in fig. 1. The diameter of tumour was found to be ~1.7 cm. The metabolic heat generation inside a breast tumour for diameter > 1 cm can be evaluated as follows: The tumour doubling time and the metabolic rate are related by hyperbolic function as $Q_{metabolic} * \tau = C$ (W day m⁻³) where, C is constant; 3.27×10⁶ (W day m⁻³) and τ is the time required for the tumour to double its volume. Further, tumour diameter (in meters) is related to τ (the time required for the tumour to double its volume) as

$$D = \exp [0.002134(\tau - 50)] \times 10^{-2} \quad (3)$$

Therefore, the metabolic heat for the tumour was calculated as 10,936 (Wm⁻³) [16]. The influence of this parameter significantly affects the temperature distribution [31].

In MNATT, the heating is induced due to Neél-relaxation losses for magnetic nanoparticles (<20 nm) and is defined through Specific Absorption Rate (SAR) which is the Q_{source}^c term in Pennes' equation [36-39]. It is measure of absorption of magnetic energy per unit volume of tumour tissue embedded with suitable magnetic nanoparticles when exposed to electromagnetic field [for formulation refer **Supplementary section-II**] [65]. In this study, SAR is averaged over the entire volume of the tumour tissue assuming uniform distribution of nanoparticles. Initially different SAR's are chosen for different blood perfusion rates to narrow down on to a specific values between 1.6×10⁶ Wm⁻³ to 2.2×10⁶ Wm⁻³ with trade-off with exposure

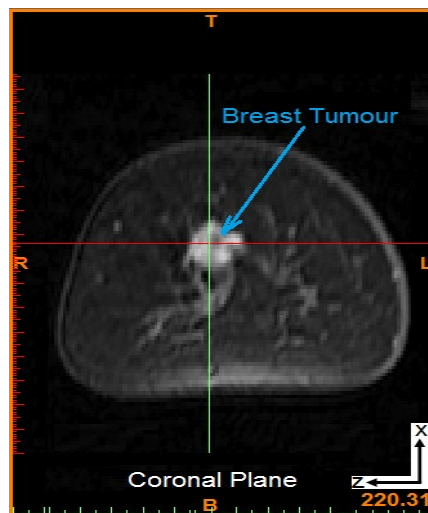
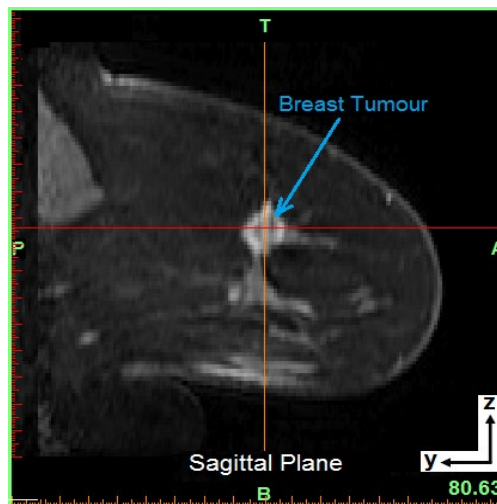
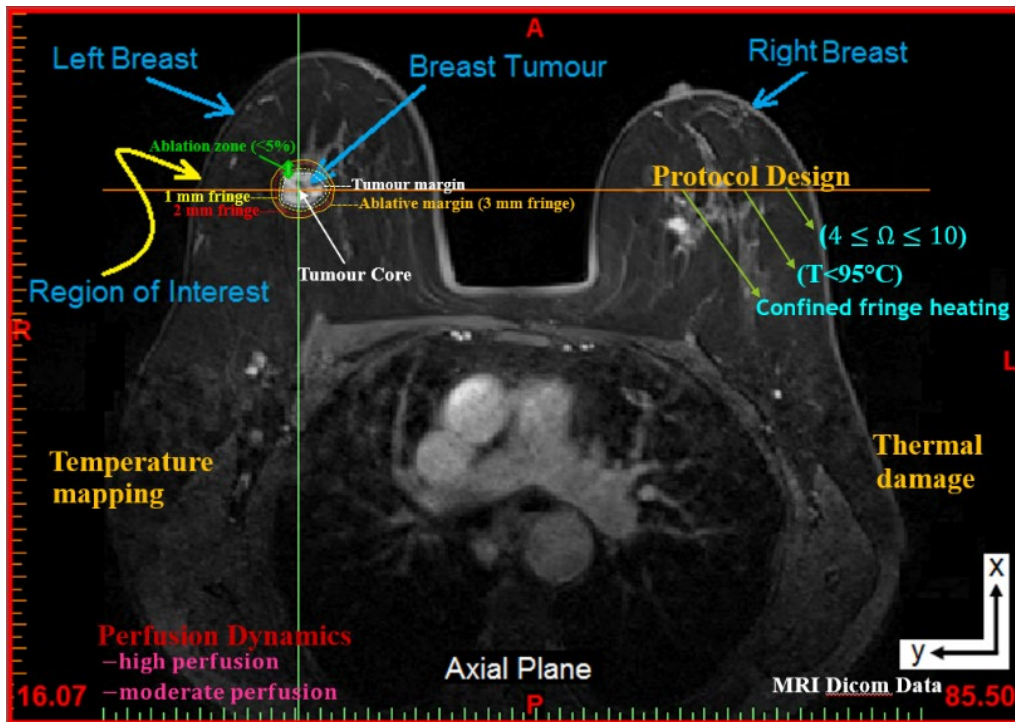


Fig. 1. MRI images of the tumour within predominantly fatty breast tissue are shown in three different views (Axial, Sagittal, Coronal). Tumour (white pixels) of 1.7 cm diameter is located within the left breast.

durations to ensure whole of the tumour is damaged considering sufficient margins.

This volumetric heat generation rate is in agreement with the recently reported magnetic nanoparticle based *in-vivo* experimental study [40]. Considering this with different variable blood perfusion conditions (blood flow within a tumour), the objective function is to map the necrosis within tumour and tumour-healthy tissue interface for the treatment duration. A number of iterative computational experiments were performed to evaluate the spatiotemporal temperature and thermal damage by choosing different values of SAR and exposure durations based on tumour blood perfusion.

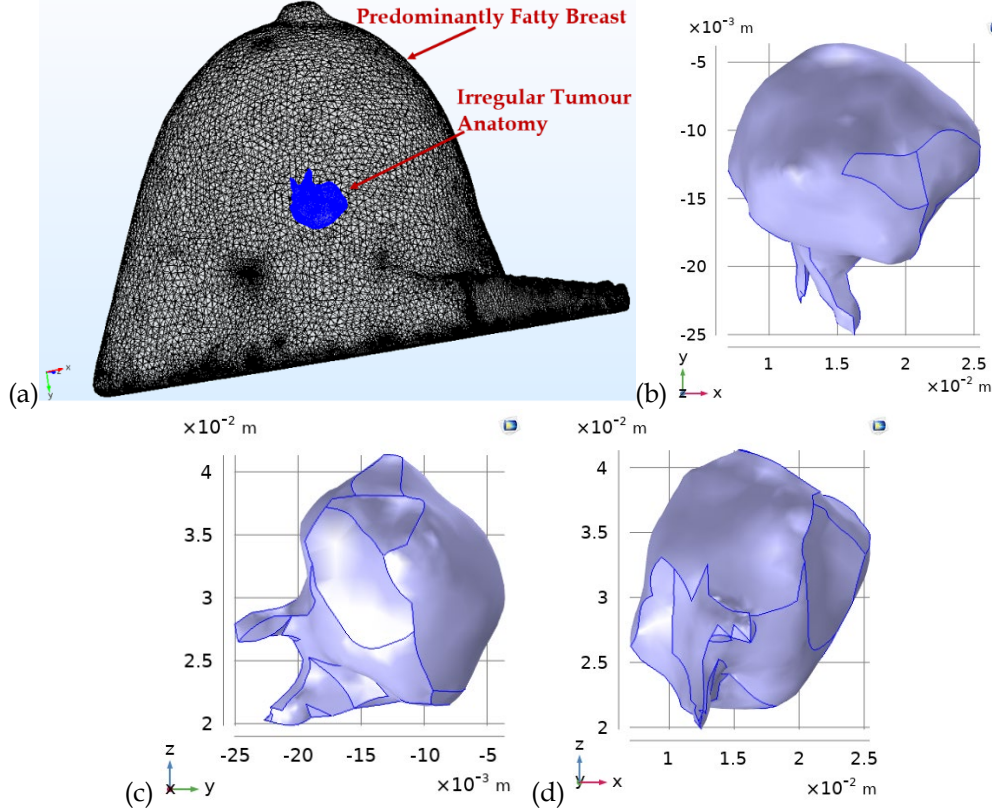


Fig. 2. Constructed geometrical details of the tissues (a) 3D two compartment meshed model of breast, (b) Breast tumour in X-Y plane (Axial), (c) Breast tumour in Y-Z plane (Sagittal), (d) Breast tumour in X-Z plane (Coronal).

2.3. Computation of thermal damage considering variable blood perfusion variation

Arrhenius model was used to evaluate thermal damage as given by Eq. (4) which accounts for both the temperature and time.

$$\Omega(x, y, z, \tau) = \ln \left\{ \frac{C(0)}{C(\tau)} \right\} = \int_{t=0}^{\tau} A e^{\left[\frac{-E_a}{R_u T_t(x,y,z,t)} \right]} dt \quad (4)$$

where, A is Frequency factor [s^{-1}], E_a is Activation energy for irreversible damage reaction [$Jmole^{-1}$] (refer **Table-II**), R_u is universal gas constant [$8.3143 Jmole^{-1}K^{-1}$], T_t is absolute tissue temperature [K] at a specific location (x, y, z) , τ is duration of exposure [seconds], $C(0)$ is original concentration of cells, $C(\tau)$ is undamaged tissue cells. Arrhenius damage parameter $\Omega=1.0$ represents 63.2% cell death while $\Omega=4$ suggests 98.2% cell death [41]. It is reported that values of

Ω exceeding 10 don't have any physical significance [42]. Therefore, thermal damage in the range of $4 \leq \Omega \leq 10$ was reported as acceptable criterion for complete tumour damage [15].

Blood flow within a tumour is an important contributing factor governing the thermal damage and thus the efficacy of magnetic nanoparticle thermal therapy based treatments. During heating, there is substantial increase in the blood perfusion within tumour due to vasodilation of capillaries and then there is decrease due to the thermal damage caused to vasculature [24]. Different models for blood perfusion, where the blood perfusion is varied as a function of temperature or thermal damage or degree of stasis, are reported in literature [15, 22-24, 43-46]. In this study, two blood perfusion conditions, for a homogeneously perfused tissue, were considered viz., (a) moderate perfusion and (b) high perfusion. Blood perfusion is varied as a function of thermal damage (Ω) as defined by Eq. (5) [22].

$$\omega_b(t) = \begin{cases} \omega_{b,0}; & \text{for } \Omega(t) \leq 0 \\ \omega_{b,0}[1 + 25\Omega(t) - 260\Omega^2(t)]; & \text{for } 0 < \Omega(t) \leq 0.1 \\ \omega_{b,0}\{\exp[-\Omega(t)]\}; & \text{for } \Omega(t) \geq 0.1 \end{cases} \quad (5)$$

where, $\Omega(t)$ is thermal damage and $\omega_{b,0}$ represents initial blood perfusion rate.

Table II: Arrhenius parameters considered in this study

Parameter	Symbol	Type of Tissue	
		Blood	Breast tissue
Activation Energy, [$Jmole^{-1}$]	E_a	4.5×10^5 [60]	$* 6.03 \times 10^5$ [24]
Frequency factor, [s^{-1}]	A	7.6×10^{66} [60]	$* 3.1 \times 10^{98}$ [24]

Source: * Thermal damage [24, 60]

2.4. Boundary conditions and numerical solution

The rate of heat loss at the surface of the breast tissue is expressed as follows

$$-k \frac{\partial T(x,y,z)}{\partial n} \Big|_{breast\ surface} = h_o(T_s(x, y, z) - T_\infty) \quad (6)$$

where, T_s and T_∞ are the breast surface temperature and ambient air temperature, respectively; h_o called surface conductance (where, $h_o = h_{conv} + h_{rad}$) which includes radiative and convective components. The combined heat transfer coefficient, h_o as reported in literature is $13.5 \text{ W/m}^2\text{C}$ [27, 47-49]. The bottom surface of the breast is the thoracic wall and which is at the core temperature of body, thus, the boundary condition in this region is $T = T_b$. Initial temperature (T_b) condition of 37°C , which is core body temperature, was imposed along with an ambient temperature (T_∞) considerations of 25°C .

Overall algorithm was implemented in commercially available Finite Element Method (FEM) based solver, COMSOL Multiphysics 5.2 (Comsol Inc., AB, Stockholm, Sweden) by importing the

volumetric mesh of patient specific breast. After assigning material properties to the domains, a grid independence study was carried out for mesh quality and computation time. Extremely fine tetrahedral mesh elements were used to discretize the physical domain and quadratic lagrangian elements were used to discretize the solution space. The numerical convergence was occurred by updating pre-specified relative tolerance to 0.001 mm. Equation based modelling approach was used to compute thermal damage while simulating the dynamic effect of blood temperature. A direct linear solver, MUMPS (Multifrontal Massively Parallel sparse direct Solver) with default pre-ordering algorithm was used for solving the temperature field. The Backward Difference Formula (BDF) was used for time marching, and care has been taken to store the data at each step by assigning strict steps for the solvers. The Newton-Raphson algorithm was used for iteration in direct solver. The temporal resolution was selected as 0.01 with a time step of one second. Regarding the mesh convergence analysis, it is observed that that lowering the temporal resolution by half resulted in a less than 0.01% change in the average temperature distribution. The five-fold increase in the mesh elements (i.e. from 133707 to 513507) resulted in a difference of less than 0.1 °C in the average temperature of tumour and less than 1% deviation in volumetric temperature of tumour domain. The adaptive time stepping scheme was used to solve time dependent problem wherein the convergence criterion was kept at 10^{-6} . Mesh Convergence analysis/Grid Independency test along with the flow chart representing the steps performed for the analysis are summarized in Table S1 and fig. S1 (refer Supplementary section-I) respectively.

2.5. Criteria/protocol for tumour treatment

A treatment protocol may be accepted if there is complete thermal damage to the tumour and less than 5% thermal damage for the surrounding healthy tissue [21, 50]. Few authors have mentioned in their work that there is problem of detecting tumour boundaries so a safety margin (fringe heating/security rim) of 10 mm is allowed in temperature range of 51-55°C [2]. In our study, a safety margin of 5 mm (from tumour boundary) is taken which is comparable with that reported for typical tumour diameter of 1.5 cm [19, 51]. Also, a fringe heating of 1-3 mm ('fringe' means distance from tumour boundary) which accounts for less than 5% damage to the healthy tissue is considered as threshold limit. The volume of the damaged healthy breast, was calculated as per Eq. (7) [46, 50] as follows:

% of damaged healthy breast tissue

$$= \left(\frac{V_{\text{damaged healthy breast}}}{V_{\text{healthy breast}}} \right) \times 100\% = \left(\frac{V_{\text{damaged healthy breast}}}{V_{\text{breast}} - V_{\text{breast tumour}}} \right) \times 100\% \quad (7)$$

Here, V is volume of tissue. Also, another protocol proposed for prostate tumours implanted in mice defines the damage to healthy tissue as per Eq. (8) [21];

$$\% \text{ Volumetric damage} = \left(\frac{V_{\text{damaged healthy breast}}}{V_{\text{breast tumour}}} \right) \times 100\% \quad (8)$$

where, $V_{\text{damaged healthy breast}}$ is volume of thermally damaged healthy tissue beyond tumour periphery and $V_{\text{breast tumour}}$ is volume of breast tumour. Thermal damage (Ω) is accounted as 10 within the tumour and $4 \leq \Omega \leq 10$ for 3 mm fringe distance beyond tumour boundary for use in Eq. (7) and Eq. (8). Both the protocols were considered for evaluation of thermal damage in the present work.

3. Results and discussion

Figs. 3a, 3b, 3c, 3d and 4a, 4b, 4c, 4d shows typical maps and contours illustrating the temporal evolution of spatial distribution of temperature and thermal damage spread over time at tumour core and tumour-healthy tissue interface regions respectively. Both perfusion considerations i.e. moderate and high perfusion are reported with an effective demarcation of required thermal-damage boundaries in healthy tissue region. Variable blood perfusion is considered as $\omega_b = 5.3 \times 10^{-2} [s^{-1}]$ for highly perfused tissue and $\omega_b = 5 \times 10^{-4} [s^{-1}]$ for moderately perfused tissue. Earlier experimental studies on electromagnetic heating of breast tumours reported temperatures above 55°C near tumour boundaries [9] which are in agreement for present perfusion considerations. The quantitative and qualitative comparisons with the literature showing possible resemblances and differences are reported in **Supplementary section-II**. After performing multiple computational experiments for a moderately perfused tumour, it is found that it is indeed difficult to attain temperatures otherwise in irregular nodal region of tumour with SAR values less than $1.5 \times 10^6 \text{ Wm}^{-3}$. So, two SAR values i.e. $1.6 \times 10^6 \text{ Wm}^{-3}$ and $1.8 \times 10^6 \text{ Wm}^{-3}$ are chosen.

Similarly for highly perfused tumour, repeated simulations suggests two SAR values of $2.0 \times 10^6 \text{ Wm}^{-3}$ and $2.2 \times 10^6 \text{ Wm}^{-3}$. Corresponding intermediate computations for the temperature and thermal damage profiles are presented in **Supplementary section-I**.

It can be seen from fig. 3 that the spatial temperature distribution in the central tumour core region is nearly symmetrical. The spatially heterogeneous temperature distribution at the vicinity of tumour peripheral regions is attributed to small variations in the thermal-diffusion-mediated heat transfer and the blood-perfusion mediated heat loss across the tumour tissue. The perfused tumour-vascular interface is considered as heat sink and has the ability to quickly dissipate heat. The irregular nodes of the tumour show small temperatures as expected for realistic cases. Insufficient thermal energy deposition in these irregular tumour nodes is probably due to the incurring significant heat loss for varying blood perfusion (between moderate and high blood flow). The small temperature changes at nodes is also evident from surface area to volume ratio relationship as indeed, it needs more time for temperature gradients to develop and propagate towards irregular nodes. Center slice plot for thermal damage mapping is shown for

1-3 mm fringe heating region adjacent to the tumour periphery suggests successful necrosis of whole tumour with clear demarcation of final layer of damage with yellow dotted line. For the moderately perfused tumour with SAR value of $1.6 \times 10^6 \text{ Wm}^{-3}$ for 218 seconds, Ω value of 10 is achieved within tumour core with corresponding temperatures of 60-95°C. From fig. 3c(ii), Ω of 10 was attained in entire tumour core with some portions of tumour having Ω value of 8-9. Previous experimental estimates of Pearce et al., 2013 [42] suggests that thermal damage higher than $\Omega \geq 10$ doesn't hold any useful significance. When $\Omega \geq 10$, i.e. $C(t) \geq e^{-\Omega} = 5 \times 10^{-5}$; thermal damage process is fully developed and no information is added by continually accumulating the Ω integral. It is a quantitative measure to show remaining undamaged tissue constituents and mapped within a cross-section of MRI slice (axial plane) for true tumour shape possessing irregular nodes which were otherwise difficult to be treated surgically.

For effective protocol design; heat propagation front once cover entire tumour zones, treatment end point was defined for prevailing perfusion in tumour. Propagation of damage is confined within 5 mm distance from tumour boundary such that Ω is 6-7 within 1 mm distance, while Ω of 3-4.5 is observed for next 2 mm distance. Beyond 3 mm, as seen from fig. 3a(ii), the thermal damage is nil with corresponding temperature of 40°C while temperature within irregular tumour region is in hyperthermic range of 45°C. Thus, the exposure duration for moderately perfused tumour is equivalent to ~4 minutes. Therefore, it can be inferred from the results of figs. 3c, and 3d that the highly perfused tumour needs higher exposure duration as well as higher SAR for propagation of thermal damage to tumour boundaries and up to 3-5 mm distance beyond tumour. The exposure duration required to ablate the highly perfused tumour is approximately double as compared to that for moderately perfused tumour.

Figs. 4a, 4b, 4c, 4d shows comparison of temperature and thermal damage focussing on the tumour boundaries and tumour irregular region. The white portion in the centre indicates that complete thermal damage is achieved on overall tumour volume. Further, the realistic breast tumour is irregular and comprises with an uneven spread in transversal (W) and longitudinal (L) directions. This patient-specific breast tumour extracted from MRI images have crests (or peaks) and troughs on surface with irregular nodes that are usually difficult to treat during surgical excision. These crests and troughs can be seen from temperature contours in fig.4a(i),4b(i),4c(i),4d(i). Thus, for the chosen SAR value for moderately perfused tumour tissue, there is negligible tumour region left with temperatures less than 43°C and thermal damage of 4 is attained. Furthermore, by increasing the SAR from $1.6 \times 10^6 \text{ Wm}^{-3}$ to $1.8 \times 10^6 \text{ Wm}^{-3}$, there is slight increase in thermal damage by an order of one at tumour boundaries while thermal damage starts propagating towards tumour irregular region.

Higher perfusion suggests longer exposure duration with an approximate 97.65% increase in exposure time as compared to moderate perfusion with an average increase of energy deposition to 22.22%. It is indeed very interesting observation that heat transfer rate is lower in

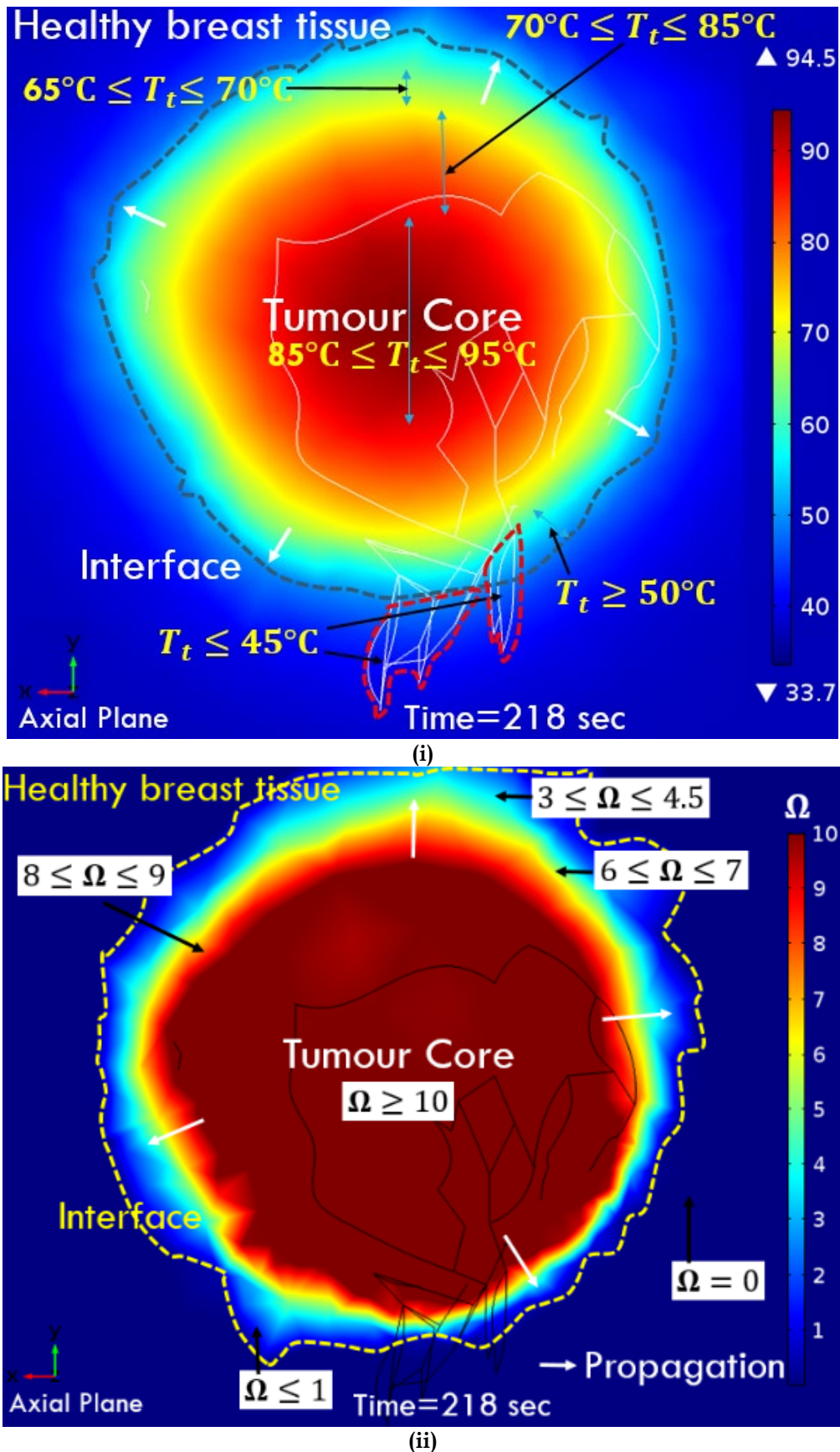


Fig. 3a. Center slice plot of temperature distribution and thermal damage at tumour core with reported SAR value of $1.6 \times 10^6 \text{ Wm}^{-3}$ at time instant of 218 sec for moderate blood perfusion as $\omega_b = 5 \times 10^{-4} [\text{s}^{-1}]$. Thermal damage is shown for 1-3 mm fringe heating region adjacent to the tumour periphery. Yellow dotted line represents final layer of damage.

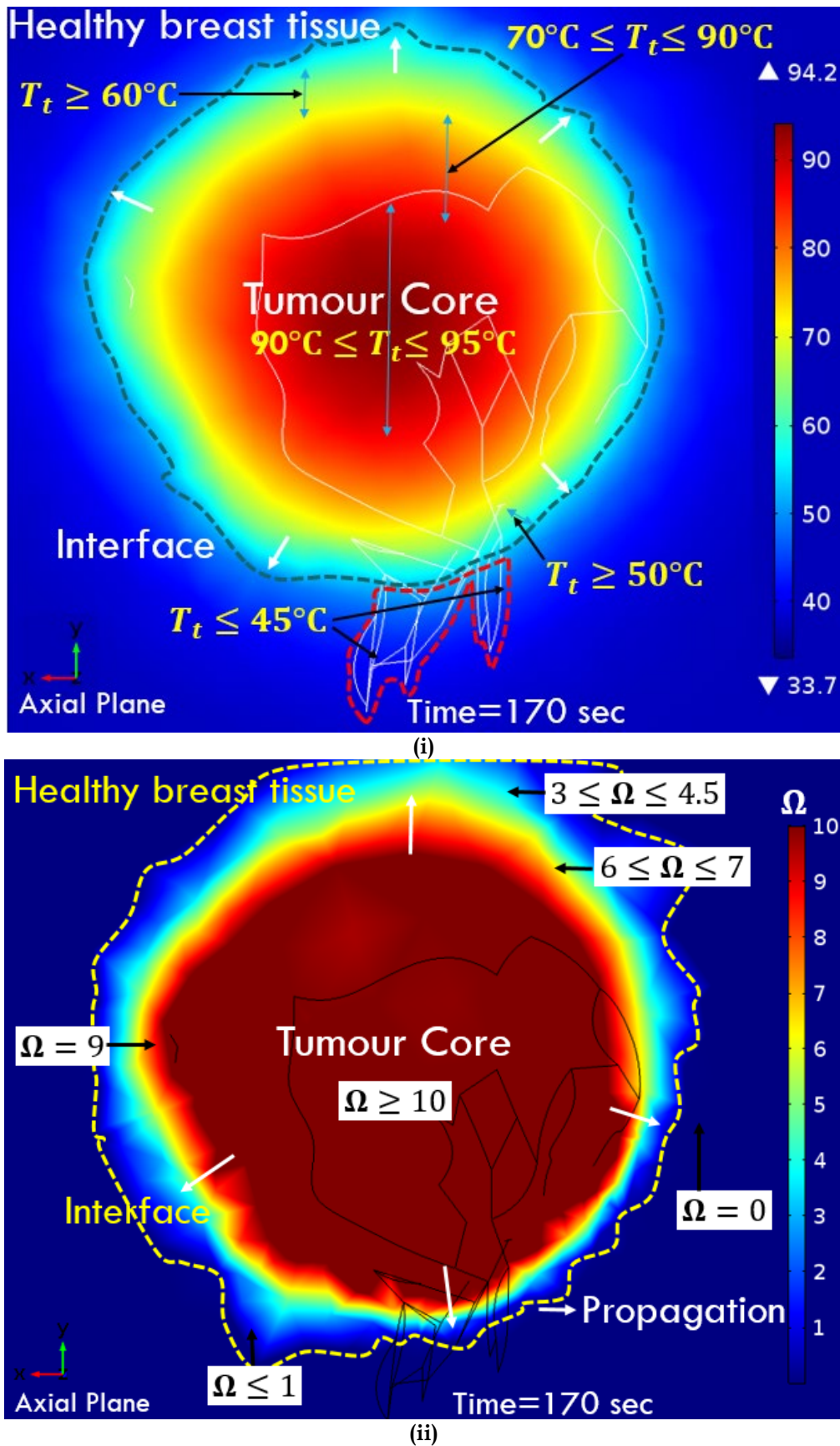


Fig. 3b. Center slice plot of temperature distribution and thermal damage at **tumour core** with reported SAR value of $1.8 \times 10^6 \text{ Wm}^{-3}$ at time instant of 170 sec for moderate blood perfusion as $\omega_b = 5 \times 10^{-4} [\text{s}^{-1}]$. Thermal damage is shown for 1-3 mm fringe heating region adjacent to the tumour periphery. Yellow dotted line represents final layer of damage.

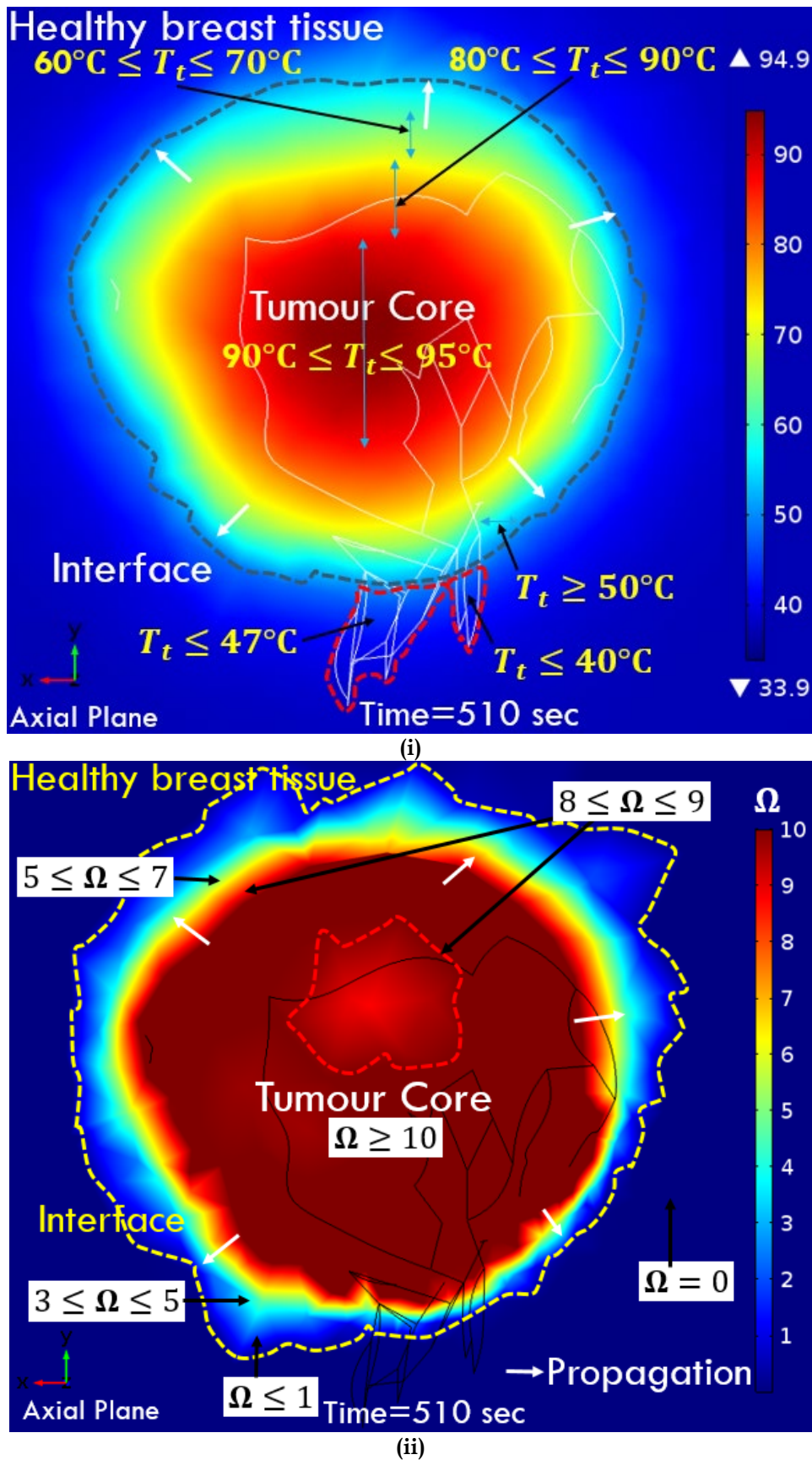
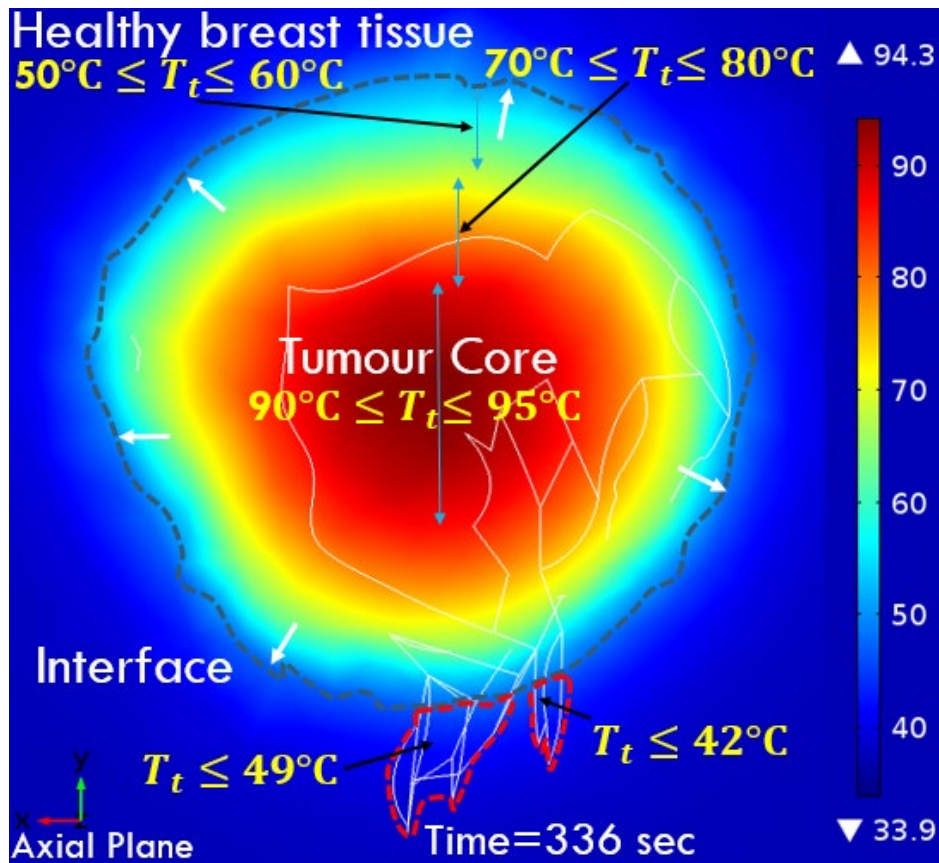
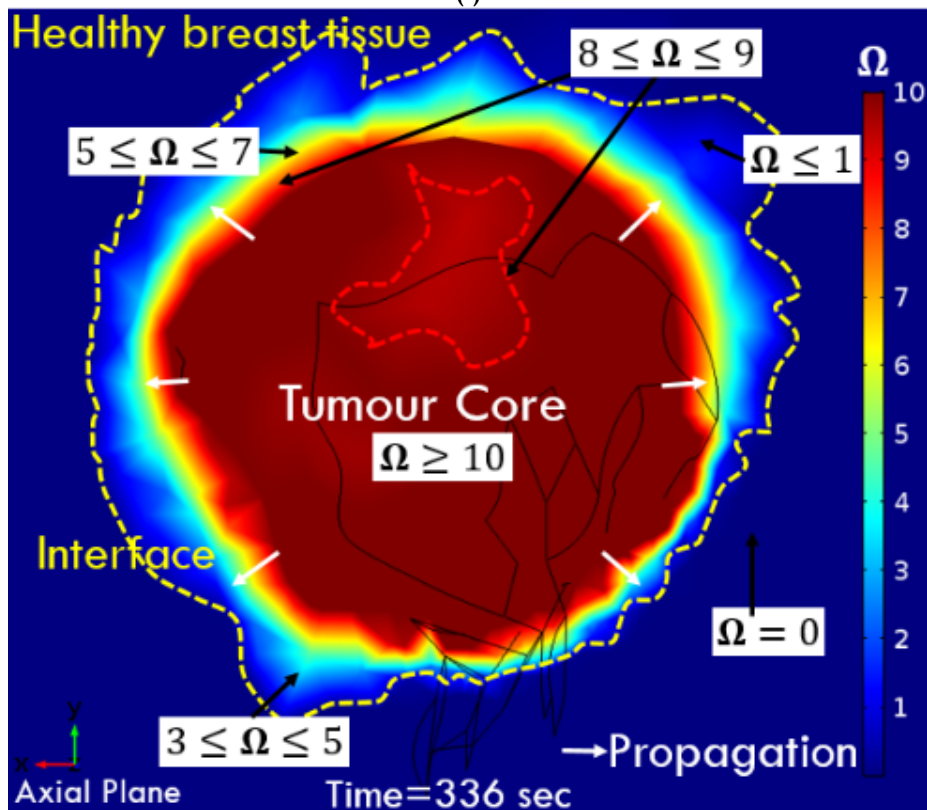


Fig. 3c. Center slice plot of temperature distribution and thermal damage at **tumour core** with reported SAR value of $2.0 \times 10^6 \text{ Wm}^{-3}$ at time instant of 510 sec for high blood perfusion as $\omega_b = 5.3 \times 10^{-2} [\text{s}^{-1}]$. Thermal damage is shown for 1-3 mm fringe heating region adjacent to the tumour periphery. Yellow dotted line represents final layer of damage.

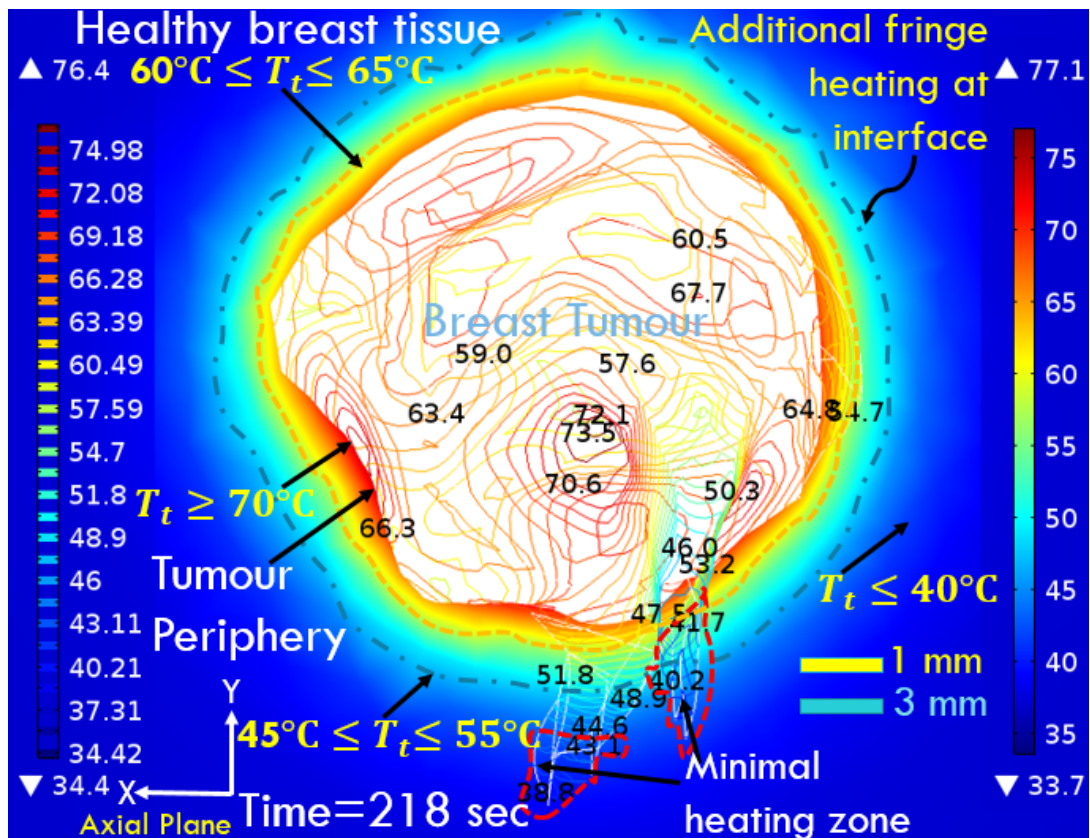


(i)

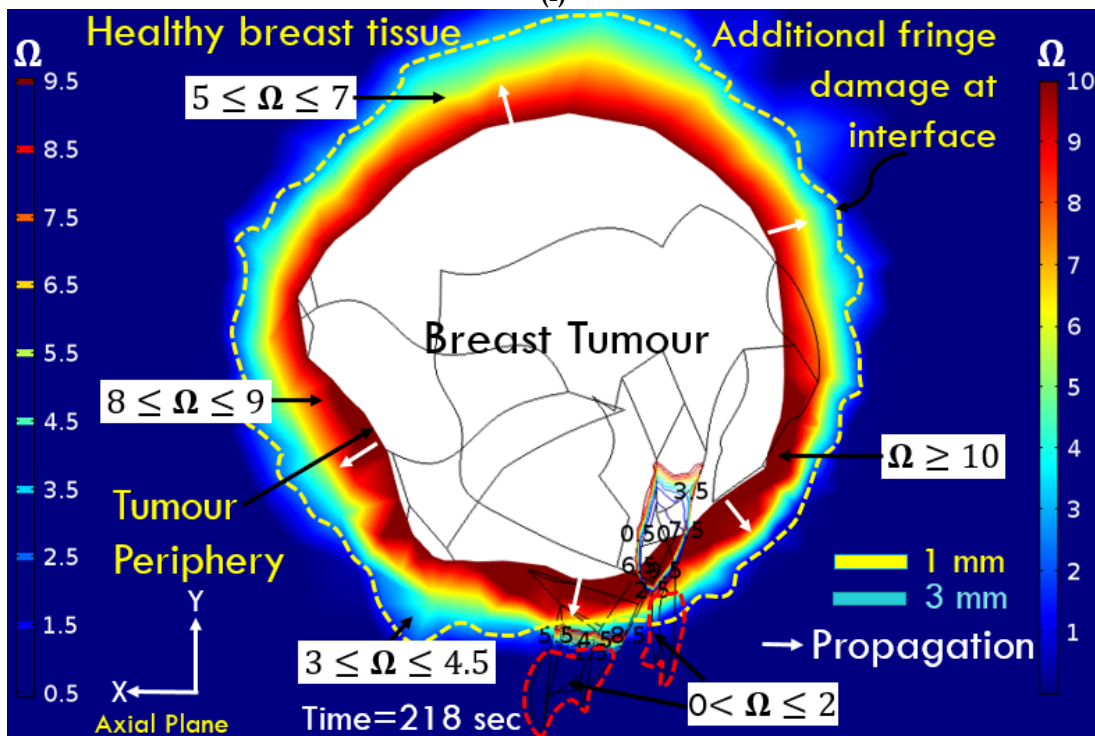


(ii)

Fig. 3d. Center slice plot of temperature distribution and thermal damage at **tumour core** with reported SAR value of $2.2 \times 10^6 \text{ Wm}^{-3}$ at time instant of 510 sec for high blood perfusion as $\omega_b = 5.3 \times 10^{-2} [\text{s}^{-1}]$. Thermal damage is shown for 1-3 mm fringe heating region adjacent to the tumour periphery. Yellow dotted line represents final layer of damage.

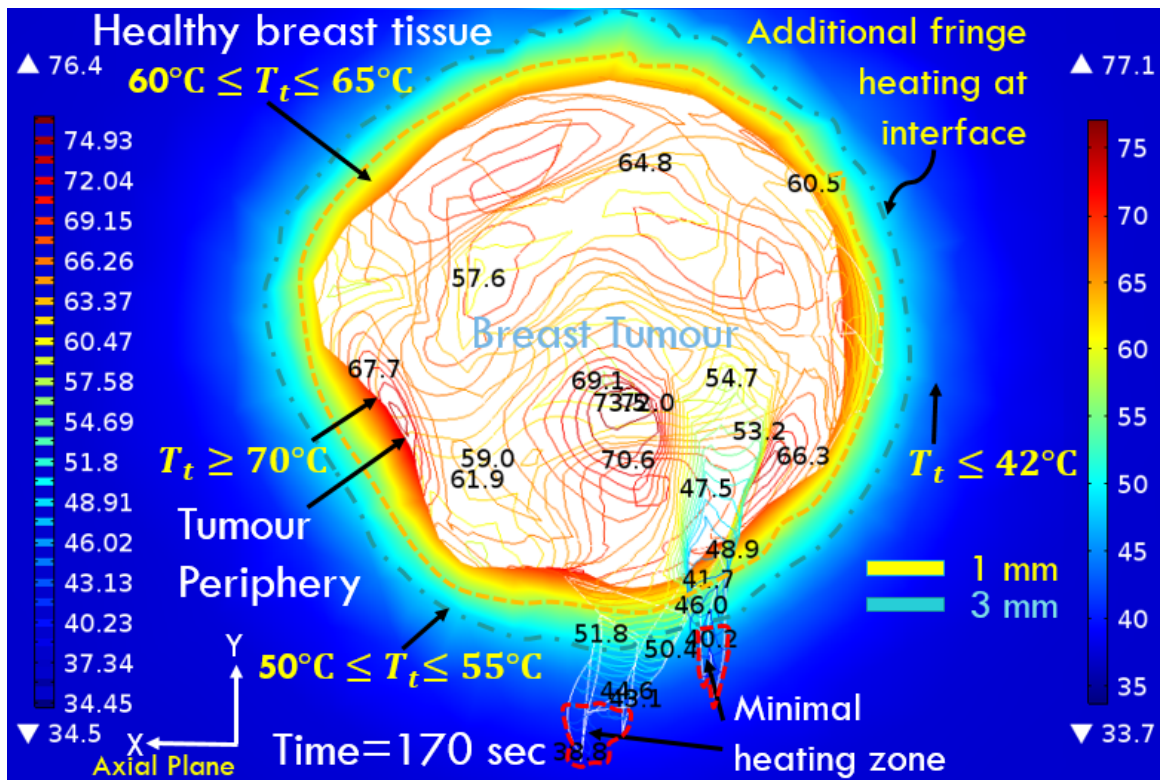


(i)

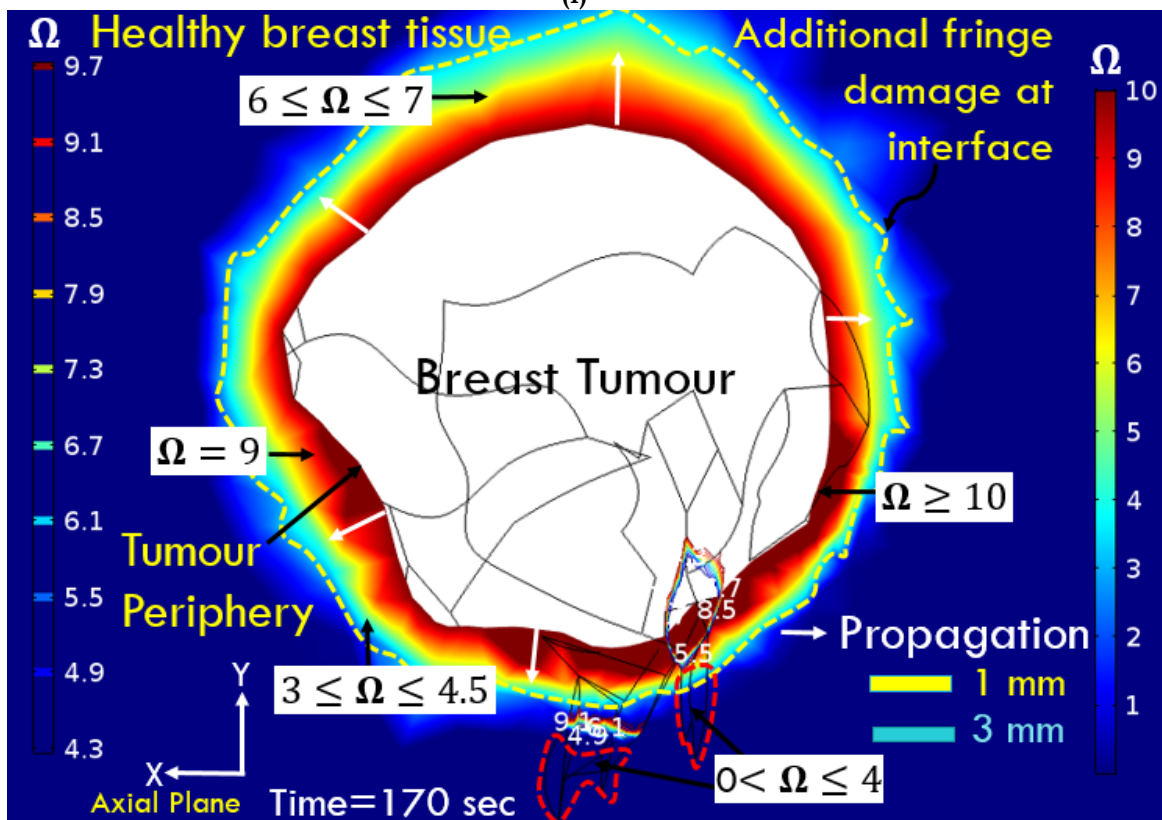


(ii)

Fig. 4a. Comparison plot of temperature distribution with thermal damage, at reported SAR values of $1.6 \times 10^6 \text{ Wm}^{-3}$, and moderate blood perfusion of $\omega_b = 5 \times 10^{-4} [\text{s}^{-1}]$ for time instant of 218 sec at **tumour interface**. Thermal damage is shown for 1-3 mm fringe heating region adjacent to the tumour periphery. Yellow dotted line represents final layer of damage. White colour surface in center of tumour shows that thermal damage spreads over the entire tumour center while surface contours over tumour irregular region show poorly heated region with mild hyperthermia temperature of 42°C .

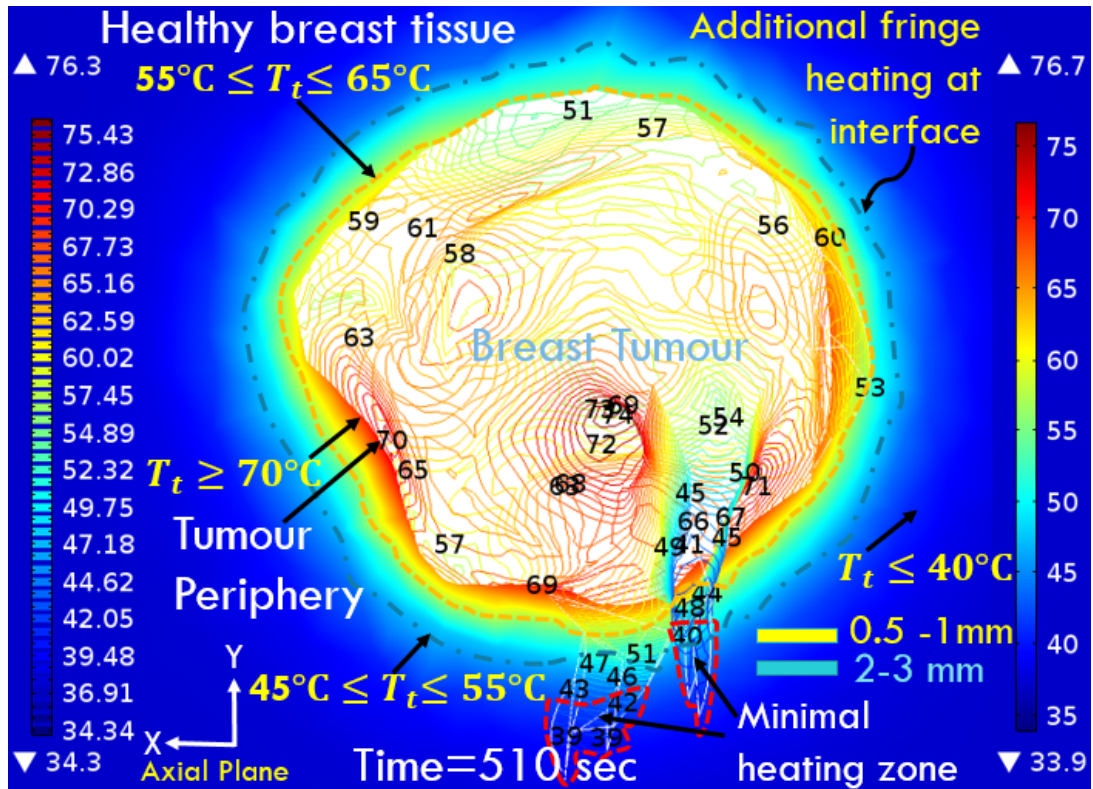


(i)

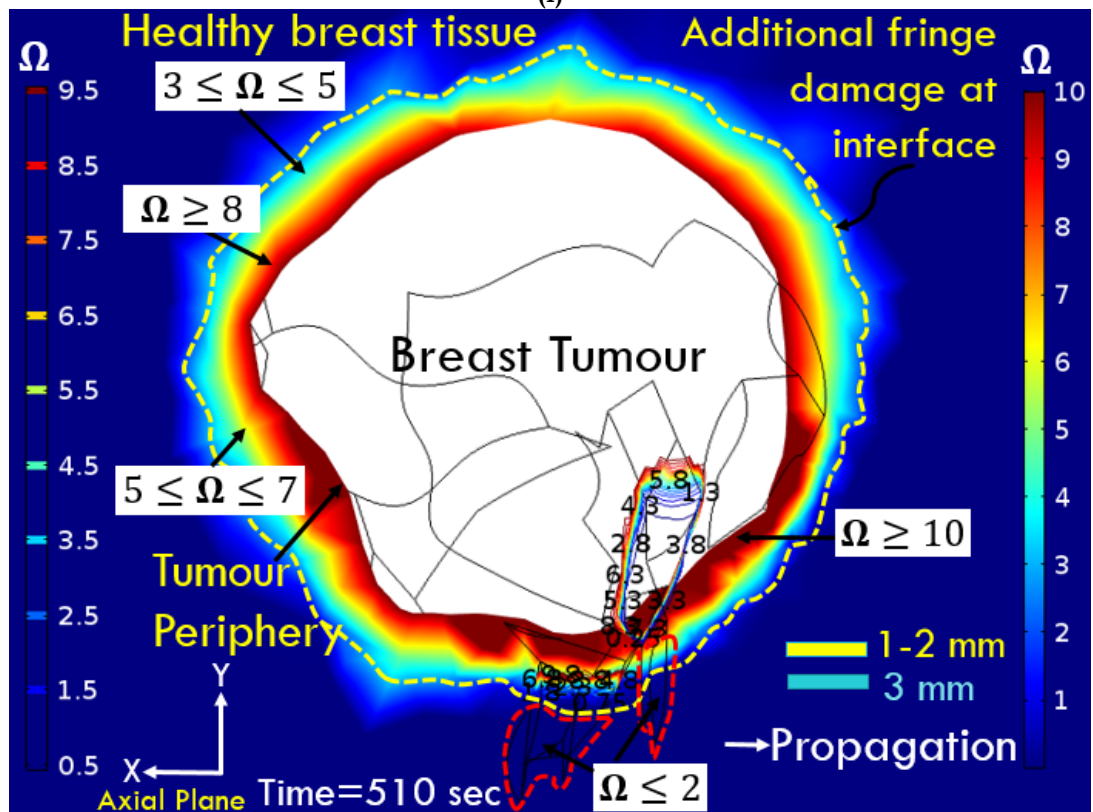


(ii)

Fig. 4b. Comparison plot of temperature distribution with thermal damage, at reported SAR values of $1.8 \times 10^6 \text{ Wm}^{-3}$, and moderate blood perfusion of $\omega_b = 5 \times 10^{-4} [\text{s}^{-1}]$ for time instant of 170 sec at tumour interface. Thermal damage is shown for 1-3 mm fringe heating region adjacent to the tumour periphery. Yellow dotted line represents final layer of damage. White colour surface in center of tumour shows that thermal damage spreads over the entire tumour center while surface contours over tumour irregular region show poorly heated region with mild hyperthermia temperature of 42°C .

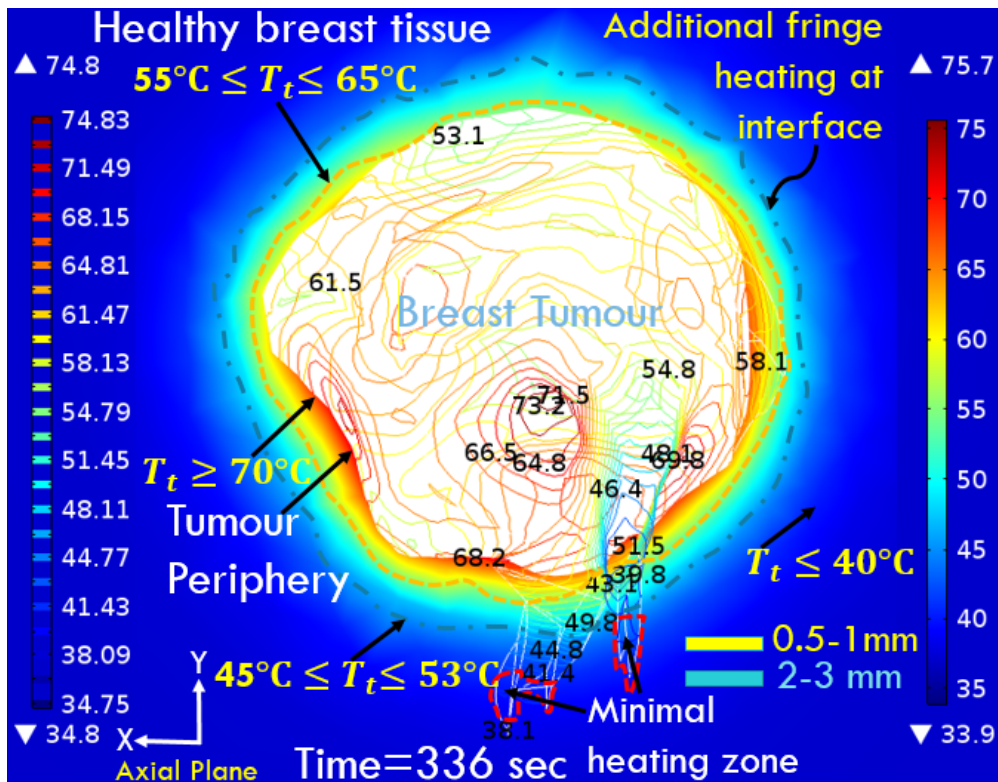


(i)

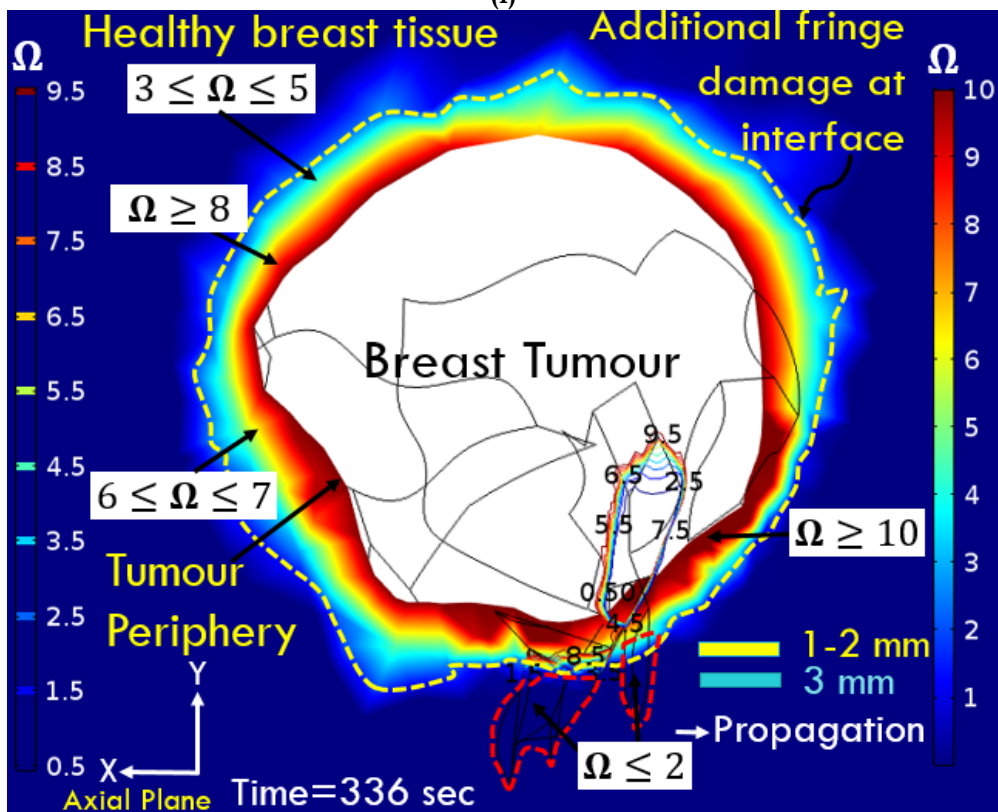


(ii)

Fig. 4c. Comparison plot of temperature distribution with thermal damage, at reported SAR values of $2.0 \times 10^6 \text{ Wm}^{-3}$, and moderate blood perfusion of $\omega_b = 5.3 \times 10^{-2} [\text{s}^{-1}]$ for time instant of 510 sec **at tumour interface**. Thermal damage is shown for 1-3 mm fringe heating region adjacent to the tumour periphery. Yellow dotted line represents final layer of damage. White colour surface in center of tumour shows that thermal damage spreads over the entire tumour center while surface contours over tumour irregular region show poorly heated region with mild hyperthermia temperature of 42°C.



(i)



(ii)

Fig. 4d. Comparison plot of temperature distribution with thermal damage, at reported SAR values of $2.2 \times 10^6 \text{ Wm}^{-3}$, and moderate blood perfusion of $\omega_b = 5.3 \times 10^{-2} [\text{s}^{-1}]$ for time instant of 336 sec at **tumour interface**. Thermal damage is shown for 1-3 mm fringe heating region adjacent to the tumour periphery. Yellow dotted line represents final layer of damage. White colour surface in center of tumour shows that thermal damage spreads over the entire tumour center while surface contours over tumour irregular region show poorly heated region with mild hyperthermia temperature of 42°C .

this nodal region as compared to rate of heat transfer in remaining tumour volume.

The moderate perfusion metrics from fig.4(a) and fig.4(b) suggests 12.5% increase in heat deposition requirements for a compensatory reduction in exposure duration by 22.02%. There is absolute no change in maximum temperature while there is an evident modification of temperature contours on irregular nodes with an even more uniform spread of heat front. For the high perfusion, it is evident from fig.4(c)-(ii) and fig.4(d)-(ii) that adjoining tumour nodes near surface has completely attained thermal damage of $\Omega \geq 4.6$ with a 10% increase in energy deposition and an average reduction in exposure duration by 34.12%. From fig. 4(c), fringes within 1 mm distance attained thermal damage, Ω of 5-7 with corresponding temperatures of 60-70°C while 47°C is achieved at tumour irregular region. For this highly perfused tumour with SAR value of $2.0 \times 10^6 \text{ Wm}^{-3}$ for 510 seconds, as shown in fig. 4(c) is 20% more than that considered for moderately perfused tumour shown in fig. 3a. By further increasing the SAR to $2.2 \times 10^6 \text{ Wm}^{-3}$, the thermal damage propagates to 5 mm distance (beyond tumour boundary in some regions) within 336 seconds as seen from fig. 3d(ii) with an effective temperature increase of 2°C in tumour irregular region i.e. 49°C is reported.

Thus, the decision regarding excessive energy deposition is based on energy balance at lowest trough and the highest crest that is balanced at the tumour surface. The effective cancer treatment protocol is based on the fact that the minimal tumour zone must develop temperatures in the hyperthermia zone while restricting damage within 3 mm distance. We estimated that the ablation tumour margins develops 50-55°C temperatures by heat conduction ensuring a safe margin which is an accepted criterion in context of breast cancer [9]. This can be well verified through visual inspection for higher perfusion metrics from fig.4(c)-(i),(ii) and fig.4(d)-(i),(ii) as it follows boundaries as per our defined function/algorithm in Comsol-Multiphysics 5.2 ensuring that the minimal thermal damage of $\Omega \geq 4.6$ is achieved. Usually the thermal ablation zone is computed as per $V = (\pi/6)LW^2$, which is an over-estimation of coagulation volume considering simpler ellipsoidal shape assumption [28, 69]. This drawback of ellipsoidal shape consideration around tumour is corrected with true boundaries rather than simply relying on 10 mm security rim and hence projecting better cosmesis for preserving the breast tissue. The designated boundaries represents voxels in 2D plane and can be extracted as three-dimensional coordinates via Comsol Multiphysics platform and mapped to original MRI image orientation and thereby ensuring effective pre-treatment planning. Those extracted voxel information can then be mapped with additional fringe damage at interface and restricted within 3 mm distance. It is evident from fig.4(c)-(i) and fig.4(d)-(i) that indeed additional 10% heat-deposition results in decrease in maximum temperature of tumour by 1°C but resulting in more uniform temperature distribution on the tumour surface. This is therefore, a trade-off between heat deposition, blood-perfusion, and exposure duration while covering whole tumour parenchyma while sparing healthy tissue fringes near the vicinity of tumour.

3.1. Estimation of tissue/necrosis volume

Breast tumour volume is approximated as 2572 mm³. Radius of tumour is approximated from the anatomical information from three principal planes (Axial/Transverse, Sagittal, and Coronal) as 8.5 mm (as per Figs. 1(b), 1(c), 1(d)). Volume of complete breast tissue is 1104000 mm³. The surface area of tumour is 1013 mm² and that of complete breast tissue is 65220 mm². Necrosis volume for 1 mm heating (beyond tumour boundary) is 1019 mm³, for 2 mm it is 2277 mm³ and for 3 mm it is 3798 mm³. The volumetric percentage of healthy breast tissue for 1 mm fringe heating reveals 0.093% thermal damage, for 2 mm fringe heating accounts to 0.21% thermal damage, for 3 mm fringe heating results in 0.34% thermal damage to healthy tissue which is well below 5% criterion. Also, the total necrosis volume including tumour and healthy tissue for 1 mm, 2 mm, 3 mm fringes are 3591 mm³ (0.33%), 4849 mm³ (0.44%), 6370 mm³ (0.58%) respectively. As these volumetric percentages are very small (<1%), which indicates successful necrosis of tumour without affecting much of the healthy breast tissue.

Fig. 5 shows the volume of damaged healthy tissue w.r.t. volume of healthy breast, calculated as per Eq. (7), within security rim of 10 mm fringe distance, with less than 5% thermal damage to healthy tissue [18,50]. This security rim is restricted to 5 mm in present analysis [19, 51]. It can be seen from fig. 5 that % volumetric damage to healthy breast is less than 1% for 3 mm fringe distance and less than 3% for 10 mm fringe distance. Overall it is less than 5%, a criterion recently reported as subjective and arbitrary definition since there is no established protocol that

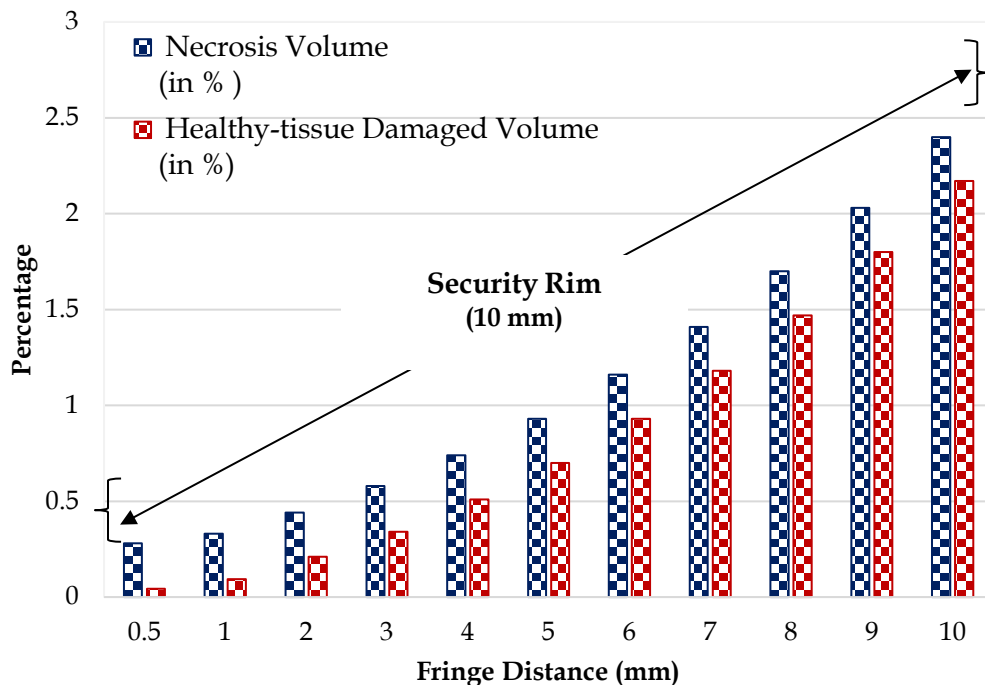


Fig. 5. Volume percentage of damaged healthy tissue tissue w.r.t. volume of healthy breast within security rim of 10 mm fringe distance beyond tumour periphery. This security rim of 10 mm margin is generally considered due to difficulty in locating tumour boundaries. Fringe distance means heating of additional healthy tissue layers surrounding tumour i.e. at tumour-healthy tissue interface that is sacrificed to avoid recurrence/reappearance.

defines acceptable amount of collateral thermal damage [21].

Fig. 6 shows in percentage, the volume of damaged healthy tissue w.r.t. tumour volume, calculated as per Eq. (8), for fringe distance beyond tumour boundary. It can be seen from fig. 6 that heating is restricted to 3 mm distance because beyond this, volume of damaged healthy tissue becomes more than 1.5 times the tumour volume. It seems the protocol as per Eq. (8) as shown in fig. 6 is better as it directly correlates with tumour volume. The analysis show that thermal damage (Ω) of 10 is achieved within entire tumour region and of 4-10 is attained beyond tumour margins ensuring the protocol that volume of damaged healthy tissue should not exceed the tumour volume.

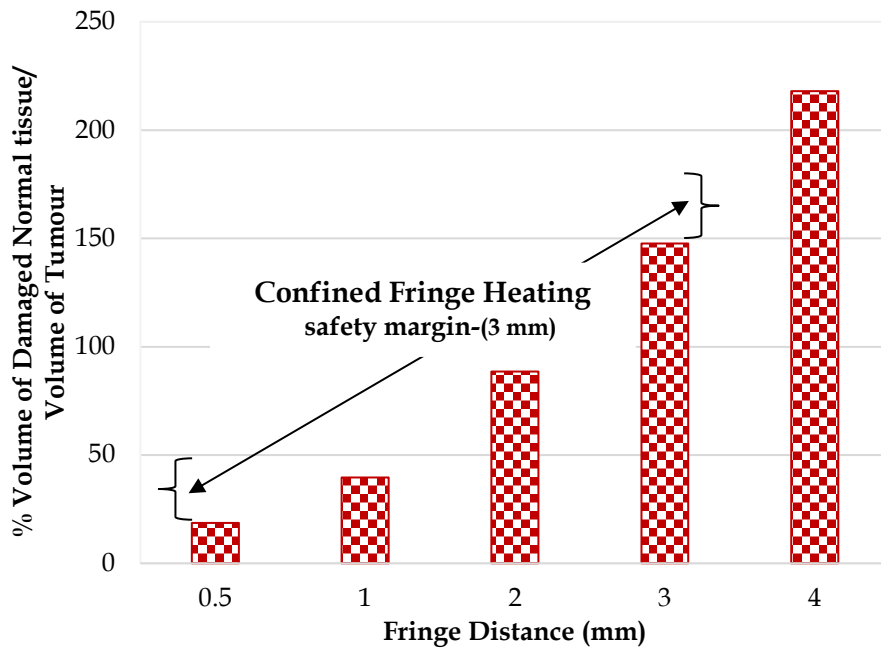


Fig. 6. Volume percentage damaged healthy tissue w.r.t. tumour volume for fringe distance beyond tumour periphery. The fringe heating is restricted to a margin of 3 mm as per the protocol designed in this study because beyond this, the thermal damage is approximately 1.5 times the tumour volume. Fringe distance means heating of additional healthy tissue layers surrounding tumour i.e. at tumour-healthy tissue interface that is sacrificed to avoid recurrence/reappearance.

As per the protocol reported in most of the thermal damage studies, a security rim of 10 mm is allowed to be thermally damaged with corresponding temperature of 50-55°C because it is difficult to map the tumour boundaries. Fewer studies report this damage within 5 mm fringe distance while other studies restrict the thermal damage within 5%. We followed the one with 5% thermal damage threshold condition, which is widely reported in previous studies. So, thermal damage to healthy tissue must remain less than 5% and also it should not exceed twice the tumour volume. Both these conditions are achieved for 3 mm distance beyond tumour periphery and corresponding SAR values and exposure duration are reported to ensure complete ablation of the considered tumour while minimising the damage beyond 3 mm of tumour boundary.

In this study, we have addressed the requirement of Specific Absorption Rate (SAR), for an irregular shaped realistic tumour, considering the variable blood flow conditions. For this, the thermal damage propagation is evaluated at the interface of tumour and peripheral healthy tissue. Despite of difficulty to incorporate complexity and additional enhancement in computational time, investigators [8, 24, 28, 52-55] did suggested non-uniform 3D breast geometries with irregular tumours as part of future investigation in order to be used in clinical scenario which was successfully addressed in present work. The detailed extensive review regarding choice of inter-relational parameters can also be referenced from Singh M., 2016 [56].

Although the effect of blood perfusion on the temperature and thermal damage has been extensively studied by some investigators using simpler geometrical assumptions of cubical, cylindrical and spherical regions. But in reality neither the tissues are cubical nor spherical but are mostly composed of irregular shape [61-62]. The current study is, to our knowledge, the first numerical investigation that compared various blood perfusion based requirements of nanoparticles to map the clinically desired irregular tumour margins that needs to be sacrificed for the conformal treatment of tumour. Given the improved quality resolution of MRI images, superimposed on MRI angiogram, patient-specific modelling may lead to the development of geometrically-accurate models that can be used by interventional radiologists to design patient-specific protocols. Simpler geometrical assumptions may lead towards underestimation or overestimation of the induced thermal coagulation volume (treatment margins) if the computational predictions are translated into patient-specific actual treatment protocols. An underestimation of thermal coagulation zone may result in over ablation while overestimation could result in incomplete ablation [57]. More recently, the importance of patient-specific modelling has been reported for liver anatomy in which exact liver shape is extracted from CT images but the shape of irregular tumour is sacrificed by manually constructing a hypothetical tumour domain [25].

The technical success of thermal ablation therapy is to fully encompass a tumour volume with adequate ablation margins while ensuring the safety of important anatomical landmarks (Organs at Risk). Both delineations (tumour and ablation zone) are projected in axial plane in present work. Our aim here, is to demarcate boundaries when it satisfies the ablation protocol for a patient-specific tumour. The literature reports a "Security Rim" of 0.5-1 cm [2-5]. Generally, 5 mm ablation margin is advised as a denominator of complete ablation. Kim et al., 2010 [73] compare-and-contrast retrospectively qualitative visual assessment with 3D quantitative assessment using CT image fusion finds that 97.3% (107/110) of the cases were failed to achieve a 5 mm ablative margin in all surrounding directions practically. Their findings using CT image fusion analysis and radial multiplanar reformation technique supports the conjecture of restricting the ablation to a 3 mm ablative margin. They postulate that where there is no space, the consideration of thinnest ablative margin (≥ 3 mm) may be considered as minimum

requirement/criterion to circumvent any further chances of tumour recurrence (LTP-Local Tumour Progression-0%). Previous experimental assisted numerical investigation on gold-nanoparticle assisted thermal ablation therapy demonstrates that it is possible to control the thermal damage within ≤ 3 mm distance from the nanoparticle region while sparing the healthy tissues fringes within 3 mm distance beyond tumour boundary for a uniform nanoparticle distribution assumption [68]. Thus, it is very important to remark that sacrificing 3 mm tissue fringes may be a subjective opinion but is very substantial where organs at risk (OR) are in near vicinity and the ablation margins > 5 mm-10 mm are not feasible as thermal damage beyond may reach the healthy anatomical structures such as in cases of Chest Wall Recurrence (CWR) [72]. Thus, we anticipate that the correlation to restrict the excessive ablation is expected to preserve for similar irregular tumour anatomies. However, this biological signature of thermal damage injury reach may seem to be intuitively correct but we still consider this as a subjective definition and the issue needs further attention to design more objective and reproducible methods to assess ablation margins.

It is certainly true to remark that the computational model becomes more robust if additional tissue compartments are added into the priori-simulations. Breast Imaging Reporting and Data System (BI-RADS) classifies breasts into four categories in the order of radiographic breast density composition namely extremely dense (ED), heterogeneously dense (HD), scattered fibroglandular (SF) and predominantly fatty (PF), wherein predominantly fatty breast is found in about 10% of women [66]. It can also be well verified from fig. 1 that the left breast, for which the results were computed, is a case of predominantly fatty (PF) breast. So, we have adopted this predominantly fatty breast composition as the base case to compute the treatment margins during magnetic nanoparticle assisted ablation therapy. Furthermore, it is reported in the literature that the temperatures are not significantly influenced by the breast density, wherein the authors used the thermal parameters of different breast densities for finite element simulations of heat transfer in biological tissue through COMSOL [67].

Kindly note that the major focus of our work is to address the irregular tumour margins. The results are sensitive to irregular tumour geometry and so the manuscript is an improvement over simplified ellipsoid, cylindrical, spherical shaped geometrical tumour assumptions generally used by researchers.

The limitations of present numerical work are, Firstly, this work was limited to only one breast scenario i.e. a female breast belonging to Class-I category. This limitation is modulated by the fact that this study aims to demonstrate the importance of computational tools, image processing (irregular tumour anatomy) rather than studying the associated complexities of variable scale within this model. For the discussed results, additional breast heterogeneities or tissue compartments may be added for a computational domain to investigate the sensitivity of thermal damage as a function of breast heterogeneity. Secondly, regarding the nanoparticle

distribution, there are multitude of studies that focus on multiple injections at several sites in tumour to attain uniform nanoparticle distribution but multiple injections may induce cracks on the surface of tumour and resulting in metastasis of cancerous cells. However, uniform nanoparticles distribution assumption taken in the present numerical computation is based on MicroCT imaging assisted experimental studies dealing with nanoparticle injection analysis. LeBrun et al., 2016 [21] reported that slower infusion rates at 3 $\mu\text{L}/\text{min}$ with single injection site resulting in repeatable uniform distribution of nanoparticles within a tumour. Furthermore, the nanoparticles undergoes redistribution and possibly migrate during low-intensive and high-intensive heating from the regions of higher concentration to the regions of low concentration due to heat mediated porosity enhancement. The numerical model will become more comprehensive if heat mediated porosity enhancement aspect can be considered by researchers working in such area. Implementation of the nanoparticle heterogeneity is out of scope of the present manuscript but this issue may be incorporated in future work. Thirdly, in the manuscript, the macro-perfusion based approach is adopted over micro-perfusion to model thermal damage as the detailed vasculature was presently missing in a given set of MRI Images and needs more contrast agent injections in patients to capture and reconstruct the detailed tumour microvasculature by using high resolution-techniques [70-71]. The possible option to incorporate the effect of blood vessels can only be addressed by acquiring MRI angiogram of breast cancer patient. In the current work, image acquisition was done at 1.0 mm slice thickness which implies that more refined information is further needed to incorporate lesser distance between slices i.e. around 0.5 mm thickness or less with a larger number of data sets (>500). Thus, the retrospective nature of present work limits the provided MRI data to moderate spatial resolution. Furthermore, this study only examines the temporal variation of blood perfusion based on thermal damage for a homogeneously perfused breast tumour tissue. However, tumours are often heterogeneous and possess leaky tortuous vessels resulting in the spatial heterogeneity of blood flow. Therefore, such an attempt of numerical computation can further be refined with inclusion of spatial heterogeneity of blood perfusion. Lastly, the thermal damage front is highly dependent on kinetic parameters i.e. Arrhenius coefficients namely activation energy and frequency factor. Only one of the widely reported values of Arrhenius coefficients are used to compute the thermal damage and therefore, appropriate range can be studied in future computational experiments to understand the significance of these coefficients and their relative effect on ablation margins.

Blood perfusion rate in breast tumours varies within an order of magnitude from 5.3×10^{-3} to $5.3 \times 10^{-2} \text{ m}^3 \text{ s}^{-1} \text{ m}^{-3}$ as reported in literature and adapted in this work [58]. Furthermore, perfusion rates in patients can be purposely modified (reduced or enhanced) via pharmacologic modulation to obtain typically considerable ablation zones. This pharmacological modulation or modification to tumour blood flow can be induced by injecting vasoactive agents or vasodepressants such as hydralazine (HYZ), phenylephrine (PE), halothane, vasopressin, or

epinephrine [45, 59]. Also, ethanol injection has been shown to augment the ablation zone by reduction of blood flow in a rat breast tumour model [74]. Thus, this preliminary work on ablation fringes using patient-specific integrated multiphysics models based on MRI-Images, can address the perfusion variation to evaluate the ablation zone dimensions. Hence, this study may serve as a link between three-dimensional pre-operative planning and post-operative assessment.

4. Conclusions

In this study, the influence of heat deposition rate (SAR), exposure duration, and variable blood perfusion metrics for a patient-specific breast tumour anatomy is quantified. The focus of the work is to evaluate the extent of tumour damage considering the tumour margins, for irregular tumour while sparing the healthy tissue. For moderately perfused tumour, SAR of $1.8 \times 10^6 \text{ Wm}^{-3}$ with exposure duration of 170 seconds is required to completely ablate the breast tumour with $\Omega=10$ at tumour core and of 4.5 at 3 mm distance beyond tumour boundary. Whereas, SAR of $2.2 \times 10^6 \text{ Wm}^{-3}$ for 336 seconds is required for tumour with high blood perfusion conditions and this exposure duration to treat highly perfused tumour, is approximately double than that for moderately perfused tumour.

The analysis show that thermal damage (Ω) of 10 is achieved within entire tumour region and of 4-10 is attained beyond tumour margins ensuring the protocol that volume of damaged healthy tissue should not exceed the tumour volume. Both the conditions (i.e. temperatures above 55°C near tumour boundaries and less than 5% thermal damage to healthy tissue) are achieved for 3 mm distance beyond tumour periphery. Corresponding SAR values and exposure duration are reported to achieve ablation of the considered tumour while minimising the damage beyond 3 mm (margin) of tumour boundary. In summary, the iterative computational experiments suggest margins less than 5 mm are sufficient enough for the given patient-specific tumour rather than sacrificing typical 10 mm excessive healthy tissue fringes criterion used clinically.

The present study is expected to unveil a deeper understanding of spatio-temporal perfusion dynamics in quantifying the tumour safety margins for magnetic nanoparticle assisted thermal therapy. Perfusion mapping derived from DCE-MRI utilizing patient-specific and site-specific tissue perfusion could allow even more accurate predictions of ablation zone dimensions. In nutshell, this study demonstrates the methodology of patient-specific medical image based computation for estimating the thermal damage especially at irregular region of tumour as well as the margin of healthy tissue to be sacrificed for magnetic nanoparticle assisted thermal therapy. This is useful for future clinical translation to predict the therapeutic region in realistic time while incorporating real tumour geometries and blood perfusion for a patient-specific tumour anatomies. The expected outcome of this work is to develop a comprehensive understanding of: (1) How does the thermal ablation zone dimensions may be affected with perfusion mediated tissue heating? (2) How does the rate of heat transfer influence the volume

of coagulation? (3) Why irregular tumour shape and boundaries are important in order to predict accurate thermal ablation margins for sparing the healthy tissues?

Acknowledgements

Authors acknowledge PGIMER Chandigarh, India for sharing the medical image data and CSIR-CSIO Chandigarh for providing computational facilities and infrastructure support. Manpreet Singh acknowledges the support of Prof. S. K. Mohapatra of Thapar Institute of Engineering and Technology University, Patiala, Punjab, India and Prof. S. S. Sehgal of Chandigarh University, Gharuan, Punjab, India.

Ethical statement

The study was entirely based on medical image data-MRI images provided by Post Graduate Institute of Medical Education and Research, Sector-12, Chandigarh, India. The access to patient's data (only one patient) was approved by the Department of Radio-diagnosis, PGIMER, Chandigarh for Computational purpose as per the Memorandum of Understanding signed between Thapar Institute of Engineering and Technology University, Patiala, Punjab, India and Post Graduate Institute of Medical Education and Research, Chandigarh, India and it was primarily approved for the partial fulfillment of the requirements of Masters in Engineering in Thermal Engineering at Thapar Institute of Engineering and Technology University, Patiala, Punjab, India in 2016.

Conflict of Interest

The authors declare that they have no competing interests.

ORCID

Manpreet Singh <https://orcid.org/0000-0003-2134-9271>

References

- 1 Hendriks P., Noortman W.A., Baetens T.R., van Erkel A.R., van Rijswijk C.S.P., van der Meer R.W., Coenraad M.J., de Geus-Oei L.F., Slump C.H., and Burgmans M.C., 2019. Quantitative volumetric assessment of ablative margins in hepatocellular carcinoma: Predicting local tumor progression using nonrigid registration software. *J. of Oncology* 4049287: 1-8.
- 2 Hilger I., Hergt R., Kaiser W.A., 2005a. Towards breast cancer treatment by magnetic heating. *J. Magn. Magn. Mater.* 293, 314-319.

- 3 Dodd III G.D., Frank M.S., Aribandi M., Chopra S., Chintapalli K.N., 2001. Radiofrequency thermal ablation: Computer analysis of the size of thermal injury created by overlapping ablations. *Am. J. Roentgenol.* 177, 777-782.
- 4 Goldberg S.N., Gazelle G.S., Mueller P.R., 2000. Thermal ablation therapy for focal malignancy: a unified approach to under-lying principles, techniques, and diagnostic imaging guidance. *Am. J. Radiol.* 174, 323-31.
- 5 Goldberg S.N., Charboneau J.W., Dodd III G.D., Dupuy D.E., Gervais D.A., Gillams A.R., Kane R.A., Lee F.T., Livraghi T., McGahan J.P., Rhim H., Silverman S.G., Solbiati L., Vogl T.J., and Wood B.J., 2003. Image-guided tumor ablation: proposal for standardization of terms and reporting criteria. *Radiol.* 228(2), 335-345.
- 6 Tani S., Tatli S., Hata N., Garcia-Rojas X., Olubiyi O.I., Silverman S.G., and Tokuda J., 2016. Three-dimensional quantitative assessment of ablation margins based on registration of pre- and post-procedural MRI and distance map. *Int. J. Comput. Assist. Radiol. Surg.* 11(6), 1133-1142.
- 7 Zorbas G., Samaras T., 2014. Simulation of radiofrequency ablation in real human anatomy. *Int. J. Hyperthermia* 30, 570-578.
- 8 Miaskowski A., Sawicki B., 2013. Magnetic fluid hyperthermia modelling based on phantom measurements and realistic breast model. *IEEE Trans. on Biomed. Eng.* 60, 1806-1813.
- 9 Hilger I., Andrä W., Hergt R., Hiergeist R., Schubert H., Kaiser W.A., 2001. Electromagnetic heating of breast tumours in interventional radiology: in-vitro and in-vivo studies in human cadavers and mice. *Radiol.* 218, 570-575.
- 10 Salloum M., Ma R., Zhu L., 2009. Enhancement in treatment planning for magnetic nanoparticle hyperthermia: Optimization of the heat absorption pattern. *Int. J. Hyperthermia* 25, 309-321.
- 11 Paulides M.M., Stauffer P.R., Neufeld E., Maccarini P.F., Kyriakou A., Canters R.A.M., Diederich C.J., Bakker J.F., Van Rhoon G.C., 2013. Simulation techniques in hyperthermia treatment planning. *Int. J. Hyperthermia* 29, 346-357.
- 12 Kok H.P., Kotte A.N.T.J., Creeze J., 2017. Planning, optimization and evaluation of hyperthermia treatments. *Int. J. Hyperthermia*, 33, 593-607.
- 13 Candeo A., Dughiero F., 2009. Numerical FEM models for the planning of magnetic induction hyperthermia treatments with nanoparticles. *IEEE Trans. Magn.* 45, 1658-1661.
- 14 Chato J.C., Gautherie M., 1990. Thermal dosimetry and treatment planning. Springer-Verlag Berlin Heidelberg.

- 15 Prakash P., Diederich C.J., 2012. Considerations for theoretical modelling of thermal ablation with catheter-based ultrasonic sources: Implications for treatment planning, monitoring and control. *Int. J. Hyperthermia* 28, 69–86.
- 16 Ng E.Y.K., Sudharshan N.M., 2001. An improved three-dimensional direct numerical modelling and thermal analysis of a female breast with tumour. *Proc. Inst. Mech. Eng.: J. Eng. Med.* H215, 25–37.
- 17 Gautherie M., Quenneville Y., Gros C.M., 1975. Metabolic heat production, growth rate and prognosis of early breast carcinomas. *Biomedicine* 22, 328–336.
- 18 Hilger I., Hergt R., Kaiser W.A., 2005b. Use of magnetic nanoparticle heating in the treatment of breast cancer. *IEEE Proc. on Nanobiotechnol.* 152, 33–39.
- 19 Nakazawa T., Kokubu S., Shibuya A., Ono K., Watanabe M., Hidaka H., Tsuchihashi T., Saigenji K., 2007. Radiofrequency ablation of hepatocellular carcinoma: Correlation between local tumor progression after ablation and ablative margin. *Hepatobiliary Imaging Am. J. Roentgenol* 188, 480–488.
- 20 Cady B., Stone M.D., McDermott W.V., Jenkins R.L., Bothe A., Lavin P.T., Lovett E.J., Steele G.D., 1992. Technical and biological factors in disease-free survival after hepatic resection for colorectal cancer metastases. *Arch. Surg.* 127, 561–569.
- 21 LeBrun A., Ma R., Zhu L., 2016b. MicroCT image based simulation to design heating protocols in magnetic nanoparticle hyperthermia for cancer treatment. *J. Therm. Biol.* 62, 129–137.
- 22 Abraham J.P., Sparrow E.M., 2007. A thermal-ablation bioheat model including liquid-to-vapor phase change, pressure-and necrosis-dependent perfusion, and moisture-dependent properties. *Int. J. Heat Mass Transf.* 50, 2537–2544.
- 23 Singh S., Bhowmik A., Repaka R., 2016. Thermal analysis of induced damage to the healthy cell during RFA of breast tumour. *J. Therm. Biol.* 58, 80–90.
- 24 Soni S., Tyagi H., Taylor R.A., Kumar A., 2015. The influence of tumour blood perfusion variability on thermal damage during nanoparticle-assisted thermal therapy. *Int. J. Hyperthermia* 31, 615–625.
- 25 Ooi E.H., Lee K.W., Yap S., Khattab M.A., Liao I.Y., Ooi E.T., Foo J.J., Nair S.R., Ali A. F.M., 2019. The effects of electrical and thermal boundary condition on the simulation of radiofrequency ablation of liver cancer for tumors located near to liver boundary. *Comp. Biol. Med.* 106, 12–23.
- 26 Zhou Y., Herman C., 2018. Optimization of skin cooling by computational modelling for early thermographic detection of breast cancer. *Int. J. Heat Mass Transf.* 126, 864–876.

- 27 Wahab A.A., Salim M.I.M., Ahamat M.A., Manaf N.A., Yunus J., and Lai K.W., 2016. Thermal distribution analysis of three-dimensional tumor-embedded breast models with different breast density compositions. *Med. Biol. Eng. Comput.* 54, 1363-1373.
- 28 Wang Z., Aarya I., Gueorguieva M., Liu D., Luo H., Manfredi L., Wang L., McLean D., Coleman S., Brown S., and Cuschieri., 2012. Image-based 3D modelling and validation of radiofrequency interstitial tumor ablation using a tissue-mimicking breast phantom. *Int. J. CARS* 7, 941-948.
- 29 Collins D.J., Padhani A.R., 2004. Dynamic magnetic resonance imaging of tumor perfusion. *IEEE Eng. Med. Biol. Magaz.* 23, 65-83.
- 30 Pennes H.H., 1948. Analysis of tissue and arterial blood temperatures in the resting forearm. *J. Appl. Physiol.* 1, 93-122.
- 31 Liu K.-C., Chen T.-M., 2018. Analysis of the thermal response and requirement for power dissipation in magnetic hyperthermia with the effect of blood temperature. *Int. J. Heat Mass Transf.* 126, 1048-1056.
- 32 Ekstrand V., Wiksell H., Schultz I., Sandstedt B., Rotstein S., Eriksson A., 2005. Influence of electrical and thermal properties on RF ablation of breast cancer: Is the tumour preferentially heated? *Biomed. Eng. Online* 4, 41.
- 33 Fujita S., Tamazawa M., Kuroda K., 1998. Effects of blood perfusion rate on the optimization of RF-capacitive hyperthermia. *IEEE Trans. Biomed. Eng.* 45, 1182-1186.
- 34 Bezerra L.A., Oliveira M.M., Rolim T.L., Conci A., Santos F.G.S., Lyra P.R.M., Lima R.C.F., 2013. Estimation of breast tumor thermal properties using infrared images. *Signal Process.* 93, 2851-2863.
- 35 Mankoff D.A., Dunnwald L.K., Gralow J.R., Ellis G.K., Charlop A., Lawton T.J., Schubert E.K., Tseng J., Livingston R.B., 2002. Blood flow and metabolism in locally advanced breast cancer: Relationship to response to therapy. *J. Nucl. Med.* 43, 500-509.
- 36 Lin C.-T., Liu K.-C., 2009. Estimation for the heating effect of magnetic nanoparticles in perfused tissues. *Int. Comm. in Heat and Mass Transf.* 36, 241-244.
- 37 Maenosono S., Saita S., 2006. Theoretical assessment of FePt nanoparticles as heating elements for magnetic hyperthermia. *IEEE Trans. Magn.* 42, 1638-1642.
- 38 Lahonian M., Golneshan A.A., 2011. Numerical study of temperature distribution in a spherical tissue in magnetic fluid hyperthermia using lattice Boltzmann method. *IEEE Trans. Nanobio.* 10, 262-68.
- 39 Zakariapour M., Hamed M.H., Fatourae N., 2017. A numerical study of magnetic nanoparticles hyperthermia with alternating magnetic field under influence of convection heat transfer. *J. Eng. Sci. Tech.* 12, 405-422.

- 40 Gu Q., Joglekar T., Bieberich C., Ma R., Zhu L., 2019. Nanoparticle redistribution in PC3 tumors induced by local heating in magnetic nanoparticle hyperthermia: In vivo experimental study. *ASME J. Heat Transf.* 141, 032402.
- 41 Henriques F.C., Moritz A.R., 1947. Studies of thermal injury in the conduction of heat to and through skin and the temperatures attained therein: A theoretical and experimental investigation. *Am. J. Pathol.* 23, 531-549.
- 42 Pearce J.A., 2013. Comparative analysis of mathematical models of cell death and thermal damage processes. *Int. J. Hyperthermia* 29, 262-280.
- 43 Lang, J., Erdmann, B., Seebass, M., 1999. Impact of non-linear heat transfer on temperature control in regional hyperthermia. *IEEE Trans. Biomed. Eng.* 46, 1129-1138.
- 44 Schutt D.J., Haemmerich D., 2008. Effects of variation in perfusion rates and of perfusion models in computational models of radio frequency tumor ablation. *Med. Phys.* 35, 3462-3470.
- 45 Wu H., Exner A.A., Krupka T.M., Weinberg B.D., Haaga J.R., 2009. Vasomodulation of tumour blood flow: Effect on perfusion and thermal ablation size. *Ann. Biomed. Eng.* 37, 552-564.
- 46 Zhang B., Moser M.A.J., Zhang E.M., Luo Y., Zhang H., Zhang W., 2014. Study of the relationship between the target tissue necrosis volume and the target tissue size in liver tumours using two-compartment finite element RFA modelling. *Int. J. Hyperthermia* 30, 593-602.
- 47 Nilsson A.L., 1987. Blood flow, temperature, and heat loss of skin exposed to local radiative and convective cooling. *J. Invest. Dermatol.* 88, 586-593.
- 48 Osman M.M., and Afify E.M., 1984. Thermal modeling of the normal woman's breast. *J. Biomech. Eng.* 106(2), 123-130.
- 49 Sudharshan N.M., Ng E.Y.K., and The S.L., 2007. Surface temperature distribution of a breast with and without tumour. *Comput. Methods Biomech. Biomed. Eng.* 2, 187-199.
- 50 Manuchehrabadi, N., Zhu, L., 2014. Development of a computational simulation tool to design a protocol for treating prostate tumours using transurethral laser photothermal therapy. *Int. J. Hyperthermia* 30, 349-361.
- 51 Singh S., Repaka R., 2017b. Temperature-controlled radiofrequency ablation of different tissues using two-compartment models. *Int. J. Hyperthermia* 33, 122-134.
- 52 Mital M., Pidarpati R.M., 2008. Breast tumor simulation and parameters estimation using evolutionary algorithms. *Model Simul. Eng.* 756436, 1-6.
- 53 Amri A., Saidane A., and Pulko S., 2011. Thermal analysis of a three-dimensional breast model with embedded tumour using the transmission line matrix (TLM) method. *Comp. Biol. Med.* 41, 76-86.

- 54 Pavel M., Gradinariu G., and Stancu A., 2008. Study of the optimum dose of ferromagnetic nanoparticles suitable for cancer therapy using MFH. *IEEE Trans. on Magn.* 44(11), 3205-3208.
- 55 Pavel M. and Stancu A., 2009a. Study of the optimum injection sites for a multiple metastases region in cancer therapy by using MFH. *IEEE Trans. on Magn.* 45(11), 4825-4828.
- 56 Singh M., 2016. Medical image assisted computational bio-heat transfer analysis of magnetic nanoparticles induced hyperthermia for breast cancer. Masters Thesis Dissertation Report, Thapar Institute of Engineering and Technology University, Patiala, Punjab, India. <http://dspace.thapar.edu:8080/jspui/handle/10266/4116>.
- 57 Breen M.S., Breen M., Butts K., Chen L., Saidel G.M., and Wilson D.L., 2007. MRI-guided thermal ablation therapy: Model and parameter estimates to predict cell death from MR thermometry images. *Ann. of Biomed. Eng.* 35(8), 1391-1403.
- 58 Vaupel P., 2009. Pathophysiology of solid tumours, in: Molls M., Vaupel P., Nieder C., and Anscher (Eds.). *The impact of tumour biology on cancer treatment and multidisciplinary strategies*, Springer Verlag, Berlin; 51-92.
- 59 Goldberg S.N., Hahn P.F., Halpern E.F., Fogle R.M., Gazelle G.S., 1998. Radio-frequency tissue ablation: Effect of Pharmacologic modulation of blood flow on coagulation diameter. *Radiol.* 209(3), 761-767.
- 60 Jia W., Choi B., Franco W., Lotfi J., Majaron B., Aguilar G., Nelson J.S., 2007. Treatment of cutaneous vascular lesions using multiple-intermittent cryogen spurts and two-wavelength laser pulses: numerical and animal studies. *Lasers in Surg. Med.* 39, 494-503.
- 61 Singh M., Gu Q., Ma R., and Zhu L., 2020. Heating protocol design affected by nanoparticle redistribution and thermal damage model in magnetic nanoparticle hyperthermia for cancer treatment. *ASME J. Heat Transfer* doi: <https://doi.org/10.1115/1.4046967>.
- 62 Singh M., Gu Q., Ma R., and Zhu L., 2019. Temperature distribution and thermal dosage affected by nanoparticle distribution in tumours during magnetic nanoparticle hyperthermia. *Proceedings of the ASME 2019 6th International Conference on Micro/Nanoscale Heat and Mass Transfer. ASME 2019 6th International Conference on Micro/Nanoscale Heat and Mass Transfer*. Dalian, China. July 8-10, 2019. V001T13A002. ASME. <https://doi.org/10.1115/MNHMT2019-4233>
- 63 Ho C.-S., Ju K.-C, Cheng T.-Y., Chen Y.-Y. and Lin W.-L., 2007. Thermal therapy for breast tumors by using a cylindrical ultrasound phased array with multifocus pattern scanning: a preliminary numerical study. *Phys. Med. Biol.* 52, 4585-4599.

- 64 Hirata A., and Fujiwara O., 2009. Modeling time variation of blood temperature in a bioheat equation and its application to temperature analysis due to RF exposure. *Phys. Med. Biol.* 54, N189-N196.
- 65 Hand J.W., 2008. Modelling the interaction of electromagnetic fields (10 MHz-10GHz) with the human body: methods and applications. *Phys. Med. Biol.* 53, R243-R286.
- 66 <https://www.cancer.gov/types/breast/breast-changes/dense-breasts>
- 67 González F.J., Ríos J., 2020, González R., Cruz O., 2020. "Effect of tissue density on the temperature pattern of the breast", *Proc. SPIE 11312, Medical Imaging 2020: Physics of Medical Imaging*, 113125J.
- 68 Soni S., Tyagi H., Taylor R.A., Kumar A., 2015. Experimental and numerical investigation of heat confinement during nanoparticle-assisted thermal therapy. *Int. Comm. in Heat and Mass Transf.*, 69, 11-17.
- 69 Ritz J.-P., Lehmann K.S., Isbert C., Reissfelder C., Albrecht T., Stein T., and Buhr H.J., 2006. In-vivo evaluation of a novel bipolar radiofrequency device for interstitial thermotherapy of liver tumors during normal and interrupted hepatic perfusion. *J. Surg. Research*, 133, 176-184.
- 70 Stamatelos S.K., Kim E., Pathak A.P., and Popel A.S., 2013. A bioimage informatics based reconstruction of breast tumor microvasculature with computational blood flow predictions. *Microvas. Research*, 91, 8-21.
- 71 Reichold J., Stampanoni M., Keller A.L., Buck A., Jenny P., and Weber B., 2009. Vascular graph model to simulate the cerebral blood flow in realistic vascular networks. *J. Cereb. Blood Flow Metab.* 29, 1429-1443.
- 72 Guiot C., Madon E., Allegro D., Piantà P.G., Baiotto B., and Gabriele P., 1998. Perfusion and thermal field during hyperthermia. Experimental measurements and modelling in recurrent breast cancer. *Phys. Med. Biol.* 43, 2831-2843.
- 73 Kim Y.-S., Lee W.J., Rhim H., Lim H.K., Choi D., Lee J.Y., 2010. The minimal ablative margin of radiofrequency ablation of hepatocellular carcinoma (> 2 and < 5 cm) needed to prevent local tumor progression: 3D quantitative assessment using CT image fusion. *Vas. and Interven. Radiol.* 195, 758-765.
- 74 Goldberg S.N., Kruskal J.B., Oliver B.S., Clouse M.S., Gazelle G.S., 2000. Percutaneous tumour ablation: increased coagulation by combining radio-frequency ablation and ethanol instillation in a rat breast tumor model. *Radiol.* 217, 827-831.



Manpreet Singh is currently a Ph.D. research scholar in the Department of Mechanical Engineering at *University of Maryland Baltimore County, Baltimore, Maryland, USA*. He is presently working on NSF funded project title "*Mild Hyperthermia to enhance delivery of therapeutic nanocarriers in tumors: imaging, in vivo study, and simulation*" and also a research intern at "*Maryland Proton Treatment Center*", *University of Maryland School of Medicine*. His research interests include Image based computational modelling approach to plan, develop and optimize protocols in clinical hyperthermia, hypothermia therapies. Singh is presently developing integrated computationally-predictive models based on in-vivo laboratory experiments on PC3 tumors to understand the interplay between different nanoparticle-mediated heat and mass transport mechanisms. His research explains the correlation among blood perfusion, permeability, porosity, interstitial fluid pressure, diffusion, accumulation, retention, penetration, and vascular tortuosity affected by heating and providing means to extrapolate the in-vivo results from mouse models to clinical applications. In 2017, he had worked with company *Capillary Biomedical Inc., California* on a NIH funded project in association with *Rowan University, New Jersey* and *Thomas Jefferson University, Pennsylvania* to design novel multi-perforated infusion catheters for type-1 diabetes patients.